Eta carinae and the homunculus: Far infrared/submillimetre spectral lines detected with the Herschel Space Observatory

Monthly Notices of the ROYAL ASTRONOMICAL SOCIETY

MNRAS **499,** 5269–5301 (2020) doi:10.1093/mnras/staa3113
Advance Access publication 2020 October 23

Eta carinae and the homunculus: far infrared/submillimetre spectral lines detected with the *Herschel Space Observatory*

T. R. Gull [1]★ P. W. Morris,[2] J. H. Black,[3] K. E. Nielsen,[4] M. J. Barlow [5] P. Royer[6] and B. M. Swinyard[5,7,8]

[1]*Code 660, Astrophysics Science Division, Goddard Space Flight Center, Greenbelt, MD 20771, USA*
[2]*California Institute of Technology, IPAC M/C 100-22, Pasadena, CA 91125, USA*
[3]*Department of Space, Earth & Environment, Chalmers University of Technology, Onsala Space Observatory, SE-43992 Onsala, Sweden*
[4]*Department of Physics, IACS, Catholic University of America, Washington, DC 20064, USA*
[5]*Department of Physics and Astronomy, University College London, Gower St, London WC1E 6BT, UK*
[6]*K. U. Leuven, Institute of Astronomy, Celestijnenlaan 200 D, BE 3001 Leuven, Belgium*
[7]*Space Science & Technology Department, Rutherford Appleton Laboratory, Chilton, Didcot, OX11 0QX Oxon, UK*
[8]*Deceased*

Accepted 2020 October 2. Received 2020 September 30; in original form 2020 March 19

ABSTRACT

The evolved massive binary star η Carinae underwent eruptive mass-loss events that formed the complex bi-polar 'Homunculus' nebula harbouring tens of solar masses of unusually nitrogen-rich gas and dust. Despite expectations for the presence of a significant molecular component to the gas, detections have been observationally challenged by limited access to the far-infrared and the intense thermal continuum. A spectral survey of the atomic and rotational molecular transitions was carried out with the *Herschel Space Observatory*, revealing a rich spectrum of broad emission lines originating in the ejecta. Velocity profiles of selected PACS lines correlate well with known substructures: H I in the central core; NH and weak [C II] within the Homunculus; and [N II] emissions in fast-moving structures external to the Homunculus. We have identified transitions from [O I], H I, and 18 separate light C- and O-bearing molecules including CO, CH, CH^+, and OH, and a wide set of *N*-bearing molecules: NH, NH^+, N_2H^+, NH_2, NH_3, HCN, HNC, CN, and N_2H^+. Half of these are new detections unprecedented for any early-type massive star environment. A very low ratio $[^{12}C/^{13}C] \leq 4$ is estimated from five molecules and their isotopologues. We demonstrate that non-LTE effects due to the strong continuum are significant. Abundance patterns are consistent with line formation in regions of carbon and oxygen depletions with nitrogen enhancements, reflecting an evolved state of the erupting star with efficient transport of CNO-processed material to the outer layers. The results offer many opportunities for further observational and theoretical investigations of the molecular chemistry under extreme physical and chemical conditions around massive stars in their final stages of evolution.

Key words: Stars: individual: Eta Carinae – stars: winds, outflows – ISM: individual objects: Homunculus – infrared: ISM – infrared: stars.

1 INTRODUCTION

Massive stars, despite their large reservoirs of hydrogen, exist for rather brief periods of time – millions of years – due to prodigious consumption of nuclear fuel necessary to counteract the huge gravitational forces.[1] The transition from main sequence to the end stage, whether it be a supernova, a black hole or other, lasts for even shorter intervals – tens to hundreds of thousands of years. These massive stars undergo a series of evolutionary changes, exhibiting specific spectroscopic characteristics (Groh et al. 2014). Instabilities occur leading to eruptive ejections that are not easily predicted. The very nearby η Car (distance 2350 pcs; Smith 2006), which underwent a massive ejection in the 1840s and a lesser ejection in the 1890s, may have undergone such a transitional phase to its current luminous blue variable (LBV) in a binary system.

The 1840s event of η Car, when its apparent magnitude brightened to rival that of Sirius, drew the attention of many astronomers (Frew 2004). Indeed, the energetics approached that of supernovae, but the erupting system survived (Davidson 1997). Modern supernova surveys detect similar events, the so-called supernova imposters, many of which precede actual supernova events by months to a few years (see e.g. Mauerhan et al. 2013). However, nearly two centuries have passed since the Great Eruption and η Car has not yet produced a supernova. Smith et al. (2018b), based upon analysis of light echoes from the 1840s event, suggest that the Great Eruption was the result of a stellar merger in a triple system leading to the current binary.

Damineli (1996) deduced a 5.5-yr periodicity defined by an extended high-ionization state and a months-long, low-ionization state of nebular and wind lines that led to the determination that η Car is a binary. Detailed studies of this massive binary, its

★ E-mail: tedgull@gmail.com

[1]Observations discussed herein were recorded with the *Herschel Space Observatory*, an ESA space observatory with science instruments provided by European-led Principal Investigator consortia and with important participation from NASA. Herein, called *Herschel*

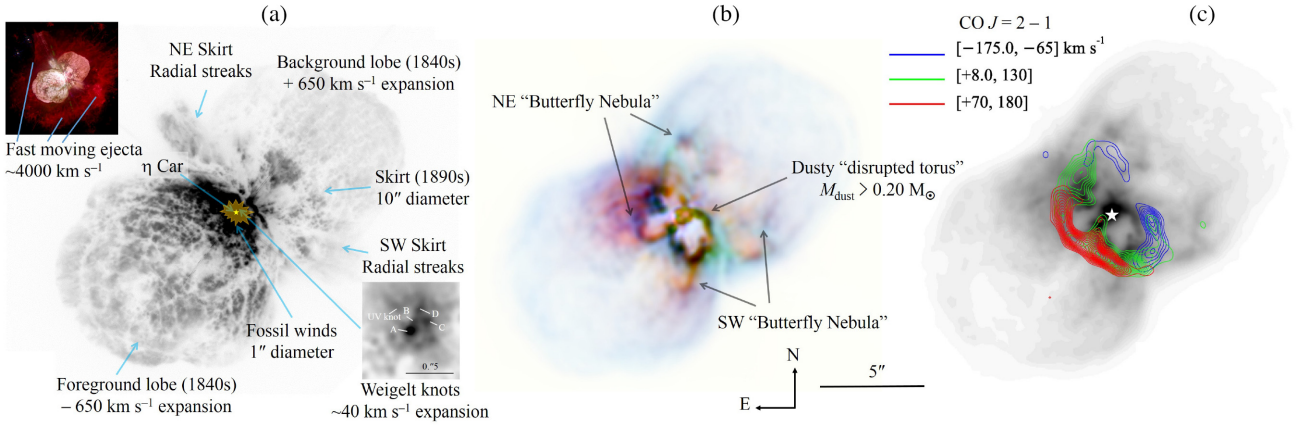

Figure 1. Ejecta structures surrounding η Car at visible, infrared, and submillimetre wavelengths are displayed with reverse relative intensity scales. The bipolar Homunculus nebula is tilted out of the sky plane by 45°, and subtends 10 arcsec × 20 arcsec in the 2011 epoch. The SE and NW lobes are expanding at −600 and +600 km s^{-1}, respectively. Much fainter, outer, irregular structures expand at space velocities approaching 6000 km s^{-1}(Smith 2008b; Kiminki, Reiter & Smith 2016). (a) Optical *HST*/ACS-HRC F660N image (Dorland 2007), showing primarily H α, [N II], and continuum radiation. The stellar fossil winds and the so-called Weigelt knots shown in the lower right inset of the central 1.3 arcsec × 1.3 arcsec region are described by Gull et al. (2016) and references therein. The outer, fast moving ejecta are accentuated in the upper left *HST* image (credit: NASA, ESA, and the SM4 ERO Team). (b) Composite *VLT*/VISIR imaging of the 13 μm (red) and 11.2 μm (green) dust band emission, and 8.98 μm [Ar III] emission (blue), from Morris et al. (in preparation). The 'Butterfly Nebula' refers to the morphology of the IR emission described by Chesneau et al. (2005). (c) Contours of CO $J = 2-1$ emission observed with *ALMA* overlaid on to a *VLT*/VISIR 7.9 μm image, from Morris et al. (2020). The emission indicated in red contours accounts for 65 per cent of the total radiated power. (red contours indicate redshifted from 0 to +140 km s^{-1}; green contours indicate redshifted from −40 to 0 km s^{-1}; blue contours indicate redshifted from −40 to −140 km s^{-1}).

ejecta, and modelling thereof have characterized the current state of the system, but have brought little understanding as to why a supernova has not yet occurred. Indeed, recent studies of the last three periastron passages suggest that the interacting winds of the massive binary were quite stable from 2000 to 2015 (Teodoro et al. 2016). Such is confirmed by the recent light-curve study by Damineli et al. (2019), who demonstrated that the apparent brightening (0.1 mag yr^{-1}) is due to dissipation of material in line of sight, but close to η Car.

Spectroscopic studies of the ejecta at visible and ultraviolet wavelengths revealed that nitrogen is very overabundant with corresponding, greatly decreased abundances of carbon and oxygen (Davidson, Walborn & Gull 1982; Davidson et al. 1986). Follow-up studies of abundances in the Weigelt blobs (Weigelt & Ebersberger 1986), ionized clumps of gas within 1000 au of η Car that appear to have been ejected in the late nineteenth century (Smith & Gehrz 1998), confirm the overabundance of nitrogen and depletion of carbon and oxygen extending the relative depletion to as much as 50- to 100-fold (Verner, Bruhweiler & Gull 2005a). Stellar evolutionary models of massive stars indicate that the ejecting star was in transition from hydrogen-burning, moving towards helium-burning, with mixing between the nuclear core and the extended outer shells, characteristic of stars more massive than 60 M$_\odot$(Ekström et al. 2012).

The luminosity of η Car, based upon early infrared measurements of the Homunculus (Westphal & Neugebauer 1969) and analysis by Cox et al. (1995), was estimated to be 5 × 10^6 L$_\odot$. Analysis, including continuum measures by *Infrared Space Observatory* (*ISO*), *Herschel* and the *Atacama Large Millimeter Array* (*ALMA*), suggested a currently lower luminosity of 3.0 × 10^{6}L$_\odot$ (Morris et al. 2017). A much more complete study by Mehner et al. (2019) recently demonstrated that the bolometric luminosity has remained stable over the past five decades, but short-term variations, likely related to the 5.54-yr binary period, could be present.

Current estimates of the binary members are that the primary, η Car A, is an LBV, exceeding 90 M$_\odot$ (Hillier et al. 2001) with a massive wind [8.5 x 10^{-4} M$_\odot$ yr^{-1} expanding at 420 km s^{-1}(Groh et al. 2012; Madura et al. 2013)] and the hot secondary, η Car B, is an O or WN star, ranging between 30 and 50 M$_\odot$ (Verner et al. 2005a; Mehner et al. 2010) with a less massive, but faster wind (1x10^{-5} M$_\odot$ yr^{-1} expanding at 3000 km s^{-1}; Pittard & Corcoran 2002). The least well known of these parameters is the total mass of the binary which is inferred from the total luminosity of the Homunculus. A recent analysis of the dynamics of the binary and interacting winds suggests a total mass exceeding 100 M$_\odot$, but is still limited by assumptions about the orbital inclination and relative luminosities of the two stars (Grant, Blundell & Matthews 2020).

Our goals with *Herschel* observations were to characterize the massive ejecta in the far-IR spectral region by molecular and atomic emission lines, to compare their spatial distributions with respect to the continuum and to inter-compare spatial and velocity properties. The angular resolution (10–30 arcsec) and the very different velocity resolutions of the instruments provide a first, coarse look at a complex system of ejecta, but further studies with higher spatial and spectral resolutions are necessary to quantify contributions of various regions.

As a guide to the reader, we display in Fig. 1 imagery in the visible and infrared spectral regions and list the following structures previously discovered by diverse studies in the visible, ultraviolet and radio spectral regions, all of which might contribute far-IR emissions:

(i) Surrounding the massive binary, η Car, which is cloaked by X-ray generating, interacting wind structures, are hemispherical shells of fossil winds that extend spatially ≈1 arcsec diameter with velocities ranging from −470 to +470 km s^{-1}) that persist for at least three binary cycles (Gull et al. 2009; Teodoro et al. 2013; Gull et al. 2016).

(ii) Within the extended fossil structures, at angular distances, 0.2–0.3 arcsec from η Car, the very slowly moving (−40 km s^{-1}), dense, partially ionized Weigelt clumps have proper motions consistent with an origin in the 1890s event (Weigelt & Kraus 2012). Multiple spectral studies demonstrated an excess of nitrogen with very little carbon and oxygen, implying they are highly processed material (Verner et al. 2005a; Mehner et al. 2010). Further studies by Teodoro

et al. (2020) indicate these clumps are bright surfaces of more extensive dusty clumps that are infrared-bright.

(iii) The radio H II region, several arcseconds in size, is offset a few arcseconds to the north-west of η Car. It grows and shrinks in synchronization with the 5.5-yr binary period (Duncan & White 2003).

(iv) The Butterfly Nebula, a cavity bounded in the near-infrared by continuum and line emission ≈3–4 arcsec in diameter, surrounds η Car, the interacting winds and the H II region (Chesneau et al. 2005). Artigau et al. (2011) found the ionized material, associable with the boundaries of the Butterfly Nebula that expands with velocities ranging from −50 to +50 km s^{-1}. The Strontium Filament, discovered by Zethson et al. (2001), is one of the brighter rims of this structure moving at −100 km s^{-1}.

(v) A molecular shell of comparable size was found to be expanding at velocities from −100 to +100 km s^{-1}. Loinard et al. (2012) identified a 'subarcsecond' molecular emitting region, in observations with the 12 m *APEX*, using arguments based upon optical depths and aperture constraints. On the other hand, Morris et al. (2017) found the size to be greater than 3 arcsec based on self-consistent modelling of the combined *APEX* (lower excitation) and *Herschel*/HIFI (higher excitation) CO spectra. More recently, Smith, Ginsburg & Bally (2018a) found a partial torus in CO (2-1) centred on η Car, looping about 2 arcsec to the east.

(vi) The Little Homunculus, an ionized, internal, bipolar structure 4 arcsec in size, expands at 200–300 km s^{-1} (Ishibashi et al. 2003).

(vii) A disrupted torus-like equatorial structure, ≈5 arcsec × 8 arcsec, observed in continuum mid-infrared (Morris et al. 1999; Polomski et al. 1999; Smith et al. 2003). This structure, internally bounded by the Butterfly cavity, lies between the two Little Homunculus lobes.

(viii) The Homunculus (the outer bipolar structures, 10 arcsec × 20 arcsec in size, as seen by scattered starlight from dust) is mapped in NIR emission lines of H_2 and Fe^+ expanding at velocities from −600 to +600 km s^{-1}(Smith 2002; Steffen et al. 2014), plus the extended skirt structures noted by Walborn, Blanco & Thackeray (1978) to the NE.

(ix) More distant, rapidly moving bullets, seen in H α and [N II], an arcminute in angular extent, move at space velocities up to 5000–6000 km s^{-1} (Weis et al. 1997; Smith 2008b; Kiminki et al. 2016; Mehner et al. 2016).

(x) Not ejecta but noticeable as background structures, the extended (2 degrees diameter), ionized Carina Nebula contributes narrow emission lines of [C II], [O II] especially notable in the 70–200 μm spectral region of PACS.

Section 2 summarizes the observations accomplished in this programme along with discussion on calibrations as this source proved to be one of the brightest objects observed with *Herschel*. Section 2.1 describes the observations and calibration of the PACS instrument and includes a list of emission lines identified with the central spaxel of the PACS. Section 2.2 describes the observations and calibration of the SPIRE data. Line identifications and spectral plots are included in Appendix A.

Section 3 presents data analysis of the PACS observations (Sections 3.1.1–3.1.8). Preliminary modelling of the SPIRE spectra is in Sections 3.2.1, 3.2.2, and 3.1.8 that address identified lines leading to abundance estimates. We found it useful to include spectral observations of η Car done with the *ISO*/Short Wave Spectrograph *SWS* in Section 3.2.4 that provided information for improved modeling of the hydrogen recombination spectrum. A summary and conclusion follows in Section 4. Appendix A displays the SPIRE spectrum and lists the line identifications.

2 OBSERVATIONS AND CALIBRATIONS

The observations presented in this paper were acquired with the two imaging spectrometers on the *Herschel Space Observatory* (Pilbratt et al. 2010) in the Open Time programme OT1_tgull_3 between 2011 August 6 and 2012 January 26, corresponding to orbit phases $\Delta\Phi$ = 0.48–0.55 on η Car's 5.54-yr period; i.e. during apastron passage with a mean separation of ≈16 au of the stellar companions. The grating spectrometer in the Photodetector Array Camera and Spectrometer (PACS; Poglitsch et al. 2010) provided wavelength coverage of 55–190 μm (1578–5454 GHz), employing two Ge:Ga photoconductor arrays. The Fourier Transform Spectrometer (FTS) of the Spectral and Photometric Imaging REceiver (SPIRE; Griffin et al. 2010) covered 194–671 μm (447–1550 GHz) with two bolometer arrays.

For our investigation into the behaviour of the far-IR/submillimetre H I Rydberg transitions observed with PACS and SPIRE, we include a mid-IR spectrum obtained with the *ISO* (Kessler et al. 1996) Short Wavelength Spectrometer (SWS; de Graauw et al. 1996). These data, obtained through large apertures in January 1996 in the S01 grating mode at spectral resolutions $R \approx$ 1200–1500 over 2.4–45.2 μm (07100250), have been presented by Morris et al. (1999, 2017), who discuss their calibrations in detail. Only the 2.4–8.0 μm range covering H I Brackett, Pfund, Humphreys, and upper state $n = 7$ series is relevant to the present study. We also include a previously unpublished high-resolution ($R \approx$ 3500) grating scan of the H I Br α 4.05 μm line, obtained in the programme `WINDS1` (29700104; PI: Martin-Pintado). Data processing methods are the same as those described by Morris et al. (2017).

As part of the our scientific rationale, certain frequency ranges were targeted for follow-up, or were augmented by existing calibration observations of η Car, with the high spectral resolution Heterodyne Instrument for the Far Infrared (HIFI; Roelfsema et al. 2012). The 490–1900 GHz range of HIFI provided good frequency overlap with SPIRE, extending to higher excitation molecular transitions and [C II] at the long wavelength end (red band) of PACS. HIFI observations of ^{12}CO and ^{13}CO, and the 450–1900 GHz continuum as observed with HIFI and SPIRE have been published in a study of the dust composition and mass in η Car by Morris et al. (2017).

2.1 PACS observations and calibration

The PACS instrument utilized a 5 × 5 array of spatial pixels (spaxels). Each of the spaxels subtends a 9.4 arcsec × 9.4 arcsec square in an irregularly spaced array on the sky as displayed in Fig. 2 projected on η Car and the Homunculus. The full width at half-maximum (FWHM) of the PACS beam at 85 μm is 9 arcsec. Spectral resolutions $\lambda/\Delta\lambda$ vary between 1500 (200 km s^{-1}) in the grating red band R1 (103–190 μm) to 2250 (133 km s^{-1}) in the two blue bands B2A (55–72 μm) and B2B (70–95 μm), and 4000 (75 km s^{-1}) in a third lower sensitivity blue band B3A (55–70 μm). For comparison, the expansion of the bipolar lobes of the Homunculus is ±600 km s^{-1}, while CO associated with the dusty disrupted torus-like structure (see Fig. 1) has velocities to roughly ±250 km s^{-1}(Loinard et al. 2012; Morris et al. 2017; Smith et al. 2018a).

The PACS observations were conducted in two visits designed to address potential issues with saturation and hysteresis of the detectors, and to determine the spatial extent of any detected emissions. The first visit, executed 2011 August 6, initially observed an OFF position 20 arcmin north-east of η Car, then at an OFFCLOSE

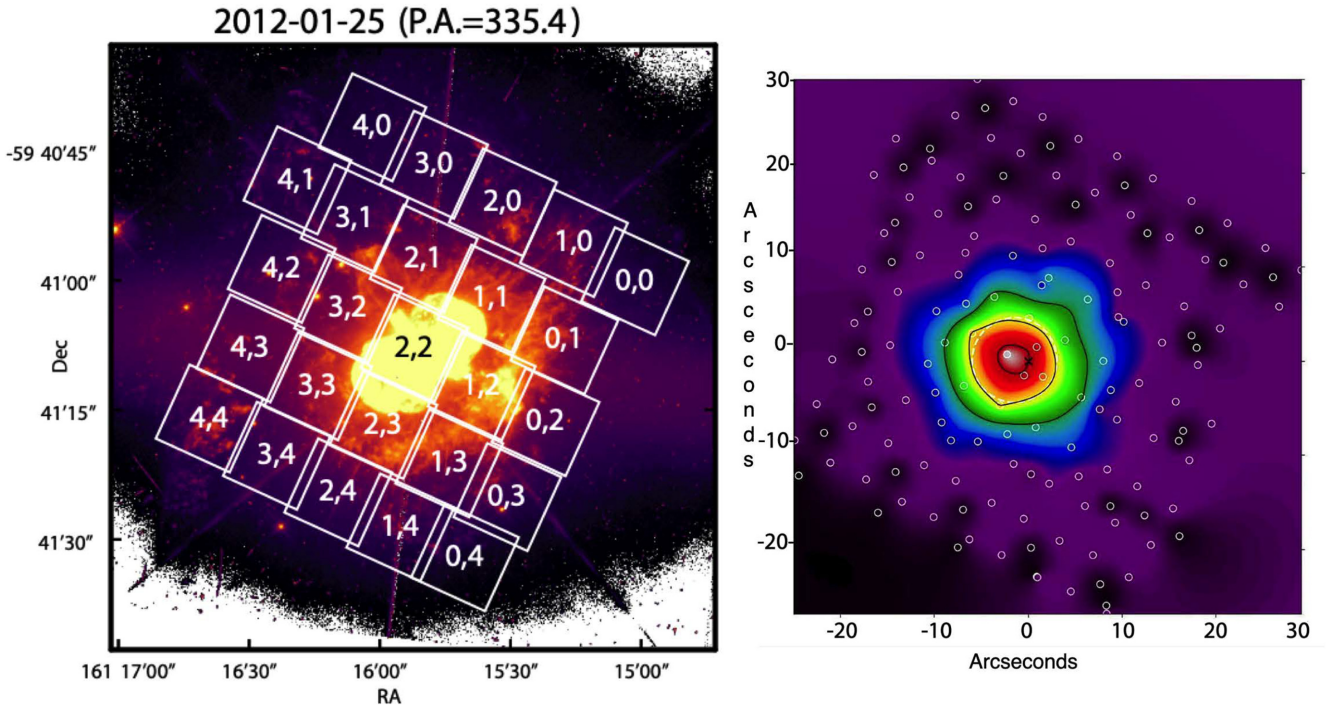

Figure 2. Placement of PACS spaxels for the visit executed 2012 January 25 (left), and a contour map of the continuum at 85 μm (right). The PACS footprint is overlaid on an *HST* image of η Car stretched in intensity. Contour levels are 0.85, 0.5, and 0.25 of the peak value. The PACS FWHM beam at 85 μm is 9 arcsec in diameter. The circles on this map depict the sampling positions of mappings accomplished during visit 2 with PACS.

position 1 arcmin north-east of η Car, and finally an ON position centred on η Car (see Table 1 for the specific offset positions from η Car). The second visit, executed on 2012 January 26, recorded grating scans centred on η Car, then repeated with four positions in a raster format using 4.5 arcsec (half-spaxel dimension) offsets from η Car.

We summarize the saturation and spectral order leakage effects on the photometric calibrations as follows:

(i) Only B2A observations were saturated; however, B3A data taken at higher spectral resolution over the same wavelength range were not.

(ii) Each position was observed by four independent scans up and down in wavelength for each selected spectral region. End portions of each scan are strongly contaminated by inter-order continuum leaks[2] (see Fig. 3). We excluded B2A data from our analysis due to the leakage and saturation. The line survey does not include 90–105 μm spectral interval due to continuum leakage.

(iii) Agreement of scans in each of B2B and B3A is generally within 5 per cent, and around 10 per cent in R1. In the interpolation between the longest B2B and shortest R1 wavelength, the maximum disagreement between these two bands is ≈30 per cent.

(iv) The level of agreement between scans in each band is likely dominated by detector dark current drifts arising from signal persistence. We estimate that measured line fluxes are uncertain by 20 per cent. Variations in fluxes between scans, as would be expected for a semi-extended point source, were noticeable in the spaxels close to the centre spaxel, labelled 2,2 in Fig. 2, left, likely due to pointing drifts. While the continuum flux map (Fig. 2) suggests the 85 μm peak may be several arcseconds east of the nominal position for η Car, this is within nominal positional accuracy for the PACS beam size and telescope pointing at this phase of the mission.

For reference, we present in Fig. 3 the observed spectral energy distribution (SED) for the central spaxel (2,2), nominally centred on η Car. The continuum from η Car and its ejecta are brightest at about 20 μm, corresponding to a dusty source of a few hundred K with a luminosity of ≈3–5 × $10^6 L_\odot$ (Westphal & Neugebauer 1969; Morris et al. 2017). At wavelengths longwards of 50 μm, this 1/λ tail of the thermal emission dominates the spectrum. Hence, the PACS spectral region emission lines are weak relative to the very bright continuum.

2.2 SPIRE observations and calibration

SPIRE-FTS spectral scans of η Car were obtained soon after the first visit with PACS as two observations with different sensitivity settings anticipating high fluxes, particularly at the blue end of the SSW module (303–674 μm). The 'nominal mode' was intended for sources with fluxes up to around 500 Jy over any portion of the available wavelength range, and consists of 25 FTS scans with a total integration time of 3330 s. Due to the risk of detector saturation at input signals above 500 Jy, a 'bright mode' observation with a total integration time of 1998 s over 40 scans was also taken at higher biasing (or 3 to 4 times lower sensitivity). Comparison of the two sets of spectra indicated that no saturation effects were present in the nominal mode spectrum and, since the nominal mode spectrum has higher S/N, well over 100 at all wavelengths, it is used for our analysis herein.

The calibrated SPIRE continuum levels were included with *ISO*/SWS, HIFI, and *ALMA* observations in a study of the unique dust spectrum of η Car by Morris et al. (2017), who provided a detailed

[2]See PACS Users Manual https://www.cosmos.esa.int/documents/12133/996891

Table 1. Log of *Herschel* observations.

Instrument mode	Date	Obs ID	Phase[a]	Spectral interval/line	Comments
PACS spectral scan[b]	2011-08-06	1342225814-822	0.463	B3A (R1), B2B (R1), B2A (R1)[c]	ON, OFF[d], OFFCLOSE[e]
PACS spectral scan[f]	2012-01-26	1342238354-359	0.549	B3A (R1), B2B (R1), B2A (R1)	ON; 1,1; 1,2; 2,1; 2,2[g]
SPIRE spectrometer[h]	2011-09-16	1342228699	0.484		15 Bright[h]
SPIRE spectrometer[h]	2011-09-16	1342228700	0.484		25 Nominal[h]

[a]Phase refers to binary phase based upon both disappearance of He I emission and X-ray drop with periastron passage on MJD 2456874.4 ± 1.3 d and orbital period of 2022.7 ± 0.3 d (Teodoro et al. 2016).
[b]The 2011-08-06 visit had the PACS array oriented at PA = 147.9°. Nominal angular resolution ranged from 9 arcsec at 57 μm to 13 arcsec at 180 μm (Bocchio, Bianchi & Abergel 2016).
[c]For each B scan, a parallel scan was done with the R grating.
[d]OFF corresponds to offset 15.8 arcmin east and 9.2 arcmin north.
[e]OFFCLOSE corresponds to offset 53 arcsec east and 46 arcsec north.
[f]The 2012-01-26 visit had the PACS array oriented at PA = 335.4° (see Fig. 2).
[g]The four observations denoted 1,1; 1,2; 2,1; 2,2 are from a set of raster scans recorded with right ascension and declination offsets 4.5 arcsec from η Car.
[h]Two sets of scans were performed: 25 FTS scans in 'nominal' mode were accomplished with a total integration time of 3330 s; 15 additional scans in 'bright-source' mode of reduced sensitivity were added for 1998 s. As no saturation effects were noted, the nominal scans with higher signal-to-noise ratio were reduced and presented in this discussion. The nominal SPIRE PSF is 18 arcsec at 190 μm and expands to 37 arcsec at 670 μm (Swinyard et al. 2010).

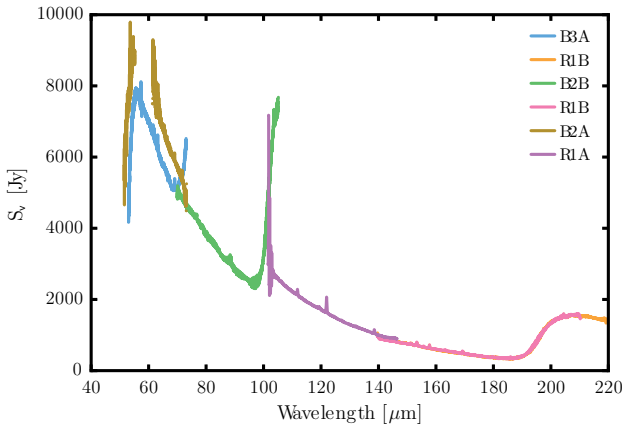

Figure 3. The SED of η Car as measured by the central spaxel (labelled 2,2 in Fig. 2). Wavelength ranges for each grating order are given in Section 2.1. η Car and its ejecta are the brightest extrasolar source at 25 μm. Hence, short wavelength continuum dominates in this spectral region, inflicting saturation in B2A and filter leakage longwards of 190 μm in the R2 spectral scan. Likewise a filter leak from third order into second order is present in B2B from 95 to 105 μm and leakage from fourth order is present in B3A longwards of 70 μm. The very small peaks against the strong continuum, as seen in the R1A and R1B spectral segments, are the stronger emission lines studied in this paper with PACS.

description of the FTS data processing. We point out here that because of the large beam sizes of SPIRE, 16.5–43 arcsec FWHM, compared to the size of the Homunculus, only one detector per section (SSWD4 and SLWC3) recorded on-source fluxes; see Fig. 2 in Morris et al. (2017) for the footprint of the SPIRE detectors during the η Car observations. The remaining off-axis detectors were used to estimate and correct for background emission.

The large discontinuity of beam sizes of the SSW and SLW modules where they overlap in wavelength produces an additional small offset in levels in the output from the central detectors, which is to be expected for point source photometric calibrations applied to a semi-extended source as η Car. This remaining offset was removed with SPIRE's semi-extended correction tool, using a Sersic brightness profile for a source 5 arcsec in diameter, which is roughly consistent with *ALMA* observations of the molecular emitting region (Morris et al. 2017). Details on the calibrations and procedures that have been followed are contained in Swinyard et al. (2010), Wu et al. (2013), Swinyard et al. (2014), Hopwood et al. (2015), Valtchanov et al. (2018), and the SPIRE handbook.[3]

Following the background and semi-extended source size corrections, we estimate continuum and line fluxes to be uncertain by ≈10 per cent in the SSW section, and somewhat higher at ≈20 per cent in the SLW section due to some departures from uniformity in the background emission.

The spectra of η Car and ejecta are plotted in Figs A1–A13. Identified lines and measured fluxes are listed in Table A1.

3 RESULTS

The *Herschel* instruments could provide only limited spatial information through direct imaging of η Car because of the angular sizes of structures within the 10 arcsec × 20 arcsec Homunculus. Fortunately, the PACS and SPIRE spectral surveys are laden with molecular and atomic emission lines, giving us a new, spectacular view into the chemistry and physical conditions of the bulk structures via emission lines from lower energy transitions. Many of these far-IR transitions are observed in η Car for the first time.

First we confirm that, as anticipated in the observation planning, the central source continuum is very strong in both sets of observations and is emitted from the massive central torus-like structure dominating mid-IR wavelengths (Morris et al. 2017; Mehner et al. 2019). Aside from the ensuing calibration issues of inter-order spectral leakage, partial saturations, and stray light during the PACS observations summarized above, the interpretations must take into account that the line and continuum emission arise from sources of varied angular extent. The coupling of the continuum radiation to the H I spectrum in the mid-IR observed with *ISO*, and the far-IR Rydberg states detected in our *Herschel* scans, is examined in Sections 3.1.8 and 3.2.4. Supported by complementary observations at higher angular and spectral resolutions, we assume for the remainder of this study that the entirety of the continuum is restricted to the central pointing of both instruments for modelling the spectral surveys, which we present below.

[3]https://www.cosmos.esa.int/web/herschel/legacy-documentation-spire

Table 2. Line identifications from the PACS spectra using the averaged central spaxel .

Identification	Measured Wave[a] (μm)	Wave number (cm^{-1})	Rest Wave[b] (μm)	Rad Vel[c] (km/s)	FWHM (km/s)	Flux[d] (10^{-15} Wm^{-2})	Comments
[N III] $^2P_{3/2}$–$^2P_{1/2}$	57.34	174.41	57.32	+90	360	22.30	Continuum leakage + fringes
NH $N = 5$–4, multiple J	61.52	162.54	61.51	+85	230	7.60	Blend $J = 6$–5, 5–4, 4–3.
[O I] $^3P_2$–$^3P_1$	63.12	158.44	63.18	−330	620	7.70	Blended
[O I] $^3P_2$–$^3P_1$	63.17	158.30	63.18	−60	125	6.57	Blended
[O I] $^3P_2$–$^3P_1$	63.21	158.21	63.18	+117	85	2.14	Blended
[O I] $^3P_2$–$^3P_1$	63.27	158.05	63.18	+426	410	5.90	Blended
CH_3OH 7_4^+–8_5^+ E1 $vt = 1 - 0$	69.00	144.93	68.98	+65	240	4.40	Tentative
H I 12–11	69.06	144.80	69.07	−50	210	7.00	.....
NH $N = 4$–3, multiple J	76.24	131.16	76.19	+190	370	2.41	Blend $J = 4$–2, 4–4
NH $N = 4$–3, multiple J	76.75	130.29	76.74	+40	600	7.73	Blend $J = 5$–4, 4–3, 3–2, 3–4
OH $N = 3^-$–2^+, $J = 7/2$–5/2	84.42	118.47	84.42[e]	0	125	1.34	.....
OH $N = 3^+$–2^-, $J = 7/2$–5/2	84.60	118.20	84.60[e]	0	270	1.70	.....
[Fe II] $a^6D_{3/2}$–$a^6D_{1/2}$	87.38	114.44	87.38	−10	200	2.60	.....
[O III] $^3P_0$–$^3P_1$	88.36	113.18	88.36	0	NR	6.18	Background Carina Nebula
unidentified	88.65	112.79	.....	.....	185	4.40	.....
H I 13–12	88.75	112.68	88.75	−10	240	5.37	.....
[Fe I] a^5D_1–a^5D_0	111.24	89.90	111.18	+150	400	1.61	Tentative; weak
H I 14–13	111.80	89.45	111.86	−140	520	6.60	.....
OH $N = 2^+$–1^-, $J = 5/2$ - 3/2	119.25	83.86	119.23	+42	265	1.08	Partial blend.
OH $N = 2^-$–1^+, $J = 5/2$ - 3/2	119.43	83.73	119.44	−10	290	1.37	Partial blend.
[N II] $^3P_1$–$^3P_2$	121.92	82.01	121.90	+65	640	17.77	Extended shell; see Fig. 6.
NH_3 $4_1 - 3_1$	127.17	78.63	127.15	+40	350	0.69	Hyperfine blend
$^{15}NH_3$ $4_3 - 3_3$	127.48	78.44	127.54	−140	NR	0.19	Tentative; weak.
H I 19–17	132.12	75.69	132.11	+3.0	300	0.56	weak
H I 15–14	138.57	72.16	138.65	−170	560	3.76	.....
[O I] $^3P_1$–$^3P_0$	145.59	68.69	145.54	+90	820	0.60	weak
NH $N = 2$–1, $J = 3$–2	153.36	65.21	153.34[f]	+25	190	1.27	NH Complex 1
NH $N = 2$–1, $J = 3$–2	153.56	65.21	153.34	+450	210	0.59	NH Complex 2
NH $N = 2$–1, $J = 2$–1	153.11	65.31	153.09	+25	190	1.00	NH Complex 1
NH $N = 2$–1, $J = 2$–1	153.33	65.31	153.09[f]	+450	210	0.37	NH Complex 2
NH_2 $3_{22} - 3_{13}$	152.85	65.42	152.92	−140	NR	0.18	.....
[C II] $^2P_{1/2}$ – $^2P_{3/2}$	157.74	63.40	157.74	0	180	0.98	∼40 per cent background.
[C II] $^2P_{1/2}$ – $^2P_{3/2}$	157.52	63.37	157.74	−420	450	0.28	Broad component (blue)
[C II] $^2P_{1/2}$ – $^2P_{3/2}$	157.52	63.37	157.74	+400	390	0.33	Broad component (red)
NH_2 $3_{13} - 2_{02}$	159.51	63.40	159.36	+280	.....	0.58	Blend 159.36, 159.53 μm
NH_2 $3_{30} - 2_{21}$	169.22	59.09	169.37	−270	120	0.70	Blended with H I
H I 16–15	169.39	59.03	169.41	−36	260	0.95	Blended with NH_2

Notes. [a]Measured wavelengths are accurate to ±0.01 μm (40 km s^{-1}) from 60 to 100 μm (order 2) and to ±0.02 μm (80 km s^{-1}) from 100 to 200 μm (order 1). Spectral resolutions vary with wavelength in each band; see Section 2.1 and the PACS Observer's Manual http://herschel.esac.esa.int/Docs/PACS/html/pacs_om.html.

[b]Vacuum wavelengths for atomic lines are from the NIST Atomic Spectra Database (https://www.nist.gov/pml/atomic-spectra-database); molecular line wavelengths are from the Cologne Database for Molecular Spectroscopy (Müller et al. 2005) and the molecular data base at the Jet Propulsion Laboratory (Pickett et al. 1998).

[c]Radial velocities are measured in the local standard of rest (LSR). NR indicates that the line is not resolved.

[d]Formal measurement uncertainties on line fluxes are 10 per cent; systematic underestimate up to 35 per cent for lines at $\lambda < 100$ μm may be caused by saturation and hysteresis effects (see Section 2.1).

[e]From Brown et al. (1982).

[f]Measurements of the line centred at 153.34 μm are based on profile decomposition using the two-component model shown in Fig. 9. Complex 1 and 2 refer to the model components shown in the figure.

3.1 PACS data analysis

3.1.1 Background, extended, and compact source emissions

While the PACS spectral mapping carried out on η Car lacks sufficient angular resolution to tie down the locations of the detected emission lines to better than ∼5 arcsec, we can deduce from each spaxel's spectral content whether the emission originates in the background Carina Nebula, or from semi-extended and compact sources within the Homunculus and central region. The expanding lobes, dusty Butterfly Nebula, and the equatorial skirt each have characteristic velocities as described above, so that the origin of most spectral features is revealed from their observed velocity structure and variations. The reader must recognize that these structures are rapidly evolving and that the fluxes are qualitative in the *Herschel* epoch of these observations.

Emission-line measurements derived from the spaxel centred on η Car (2,2) are listed in Table 2. As described above, many lines originate from extended structures, fast-moving ejecta and/or background ionized gas. The lines are relatively weak compared to continuum, and were measured in each of the six scans centred

or with subspaxel offsets from η Car. We applied the standard line detection condition for the measured intensities, namely $3\sigma = 3 \times \sigma_{\rm RMS}\sqrt{2\Delta v_{\rm bin}\Delta v_{\rm FWHM}}$, where $\sigma_{\rm rms}$ is the rms noise of the line-free baseline, $\Delta v_{\rm bin}$ is the channel binning width in km s^{-1}, and $\Delta v_{\rm FWHM}$ is the full width at half-maximum intensity of the spectral line fitted as a Gaussian profile.

The line fluxes listed in Table 2 are measured using the 9.4 arcsec × 9.4arcsec spaxel sampling the PACS point spread function (PSF) that changes in each band. The formal measurement uncertainties are around 10 per cent. Because of near saturation due to the strong continuum, however, we are unable to provide a total flux for these emission lines since the flux for the central spaxel may be depressed by up to 35 per cent, especially in the blue bands, compared to the fluxes in adjacent spaxels.

Examination of the spectral-line distribution in the PACS maps readily reveals the origin on the scales of the major features of η Car:

(i) The atomic emission lines of [O I], [O III], [C II], and [N II] contribute background emission, as expected from many previous studies of the Carina Nebula;
(ii) Emission from the outer, fast moving 'bullets' is detected in [N II];
(iii) Semi-extended emission of [O I], [O III], [C II], [Fe II], and [N II] in the Homunculus;
(iv) H recombination emission from the central region;
(v) Molecular emission from OH, NH, NH_2, NH_3, and tentatively CH_3OH from the central region and Homunculus.

We discuss the observed spectral characteristics of these features next.

3.1.2 [O I] 63.18 μm and [O III] 88.36 μm

The [O III] line provides a useful reference for consistency between spaxels (Fig. 5), as it originates entirely from the background Carina Nebula extending over several degrees. Measures of the line flux, peak wavelength, and FWHM are nearly constant over the entire 45 arcsec × 45 arcsec map, except on the central spaxel where the line flux drops nearly twofold compared to the other 24 spaxels. This suppression may be caused by near-saturation of the central spaxel, particularly at the blue end of the spectrum. As a consequence, we cannot judge if there is any contribution from η Car. However, nebular [O III] is not expected in the Homunculus since (1) no [O III] nor [O II] lines have been detected at visible wavelengths from the Homunculus (Davidson et al. 1986; Verner et al. 2005a; Zethson et al. 2012); and (2) Smith & Morse (2004) found no visible [O III] near the Homunculus, but increasing amounts detected at tens of arcseconds distance. This decrease in the infrared [O III] centred on η Car is likely the result of the massive winds and ejecta, both greatly depleted of oxygen, clearing oxygen from the immediate surroundings.

[O I] is detected in η Car, and in contrast to [O III], the profile on the central source is resolved and surprisingly structured with at least four velocity peaks; see Fig. 4, where we present the [O I], [N II], and [C II] spectra measured on the central spaxel and from the background in the insets. We discuss the extended structure of [N II] and [C II] below. Previously, only very weak [O I] was identified in the spectrum of the Weigelt condensations (Zethson et al. 2012), within ∼0.5 arcsec central source. [C II] has been observed with HIFI (Morris et al. 2017) but rendered uncertain in profile properties by the off-source chopping of the clumpy background. Here all three profiles share similar velocity structure, with a resolved central component originating from the central region including the Butterfly Nebula, and broad blue- and red-shifted components originating from the expanding lobes and possibly the equatorial skirt.

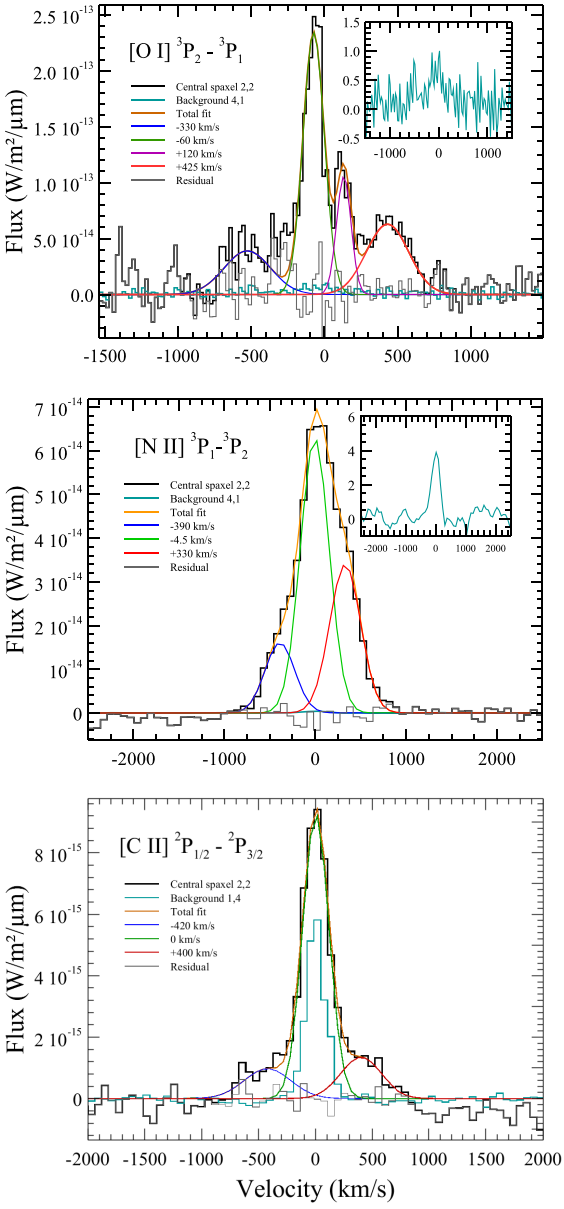

Figure 4. [O I], [N II], and [C II] line profiles on η Car. The observed spectra in the central spaxel (2,2), continuum subtracted, are shown with Gaussian profile decomposition, demonstrating the similarities in velocity structure with broad red and blue wings and a strong spectrally resolved central component (see Table 2). Extended background emission from outer spaxels for each line is shown for comparison by the cyan coloured spectra, on scales of 10^{-14} and 10^{-16} W m^{-2} μm^{-1} for [O I] and [N II], respectively. Only background [C II] contributes significantly to the central spectrum, ≈40 per cent to the total central component. The background [O I] and [C II] lines are unresolved, while [N II] is broadened by an extended shell around η Car (see the text).

Only in the [C II] line is there a significant contribution from the background, ∼40 per cent of the total line flux. The local standard of rest (LSR) velocities match expectations for the Carina Nebula: [O I] and [C II] background lines have measured velocities $v_{\rm LSR} = -20$ and 0 km s^{-1}, respectively, in good agreement with SOFIA/GREAT

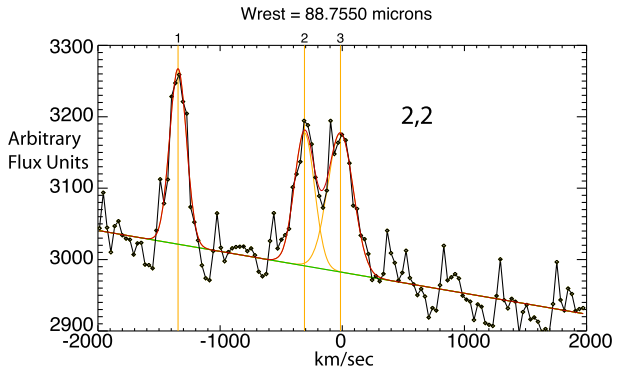

Figure 5. H I 13-12 (88.755 μm) line profile measured by PACS, centred on η Car. The line labelled '1' corresponds to background [O III] 88.36 μm. The H I emission feature labelled '3' is blended with an unidentified transition, labelled '2'. LSR velocities are referenced to the H I 13-12 rest wavelength. The line is detectable within only four spaxels, strong on spaxel 2,2, and weak in three nearby spaxels which is consistent with a nearly point-like source compared to the PACS spatial response. The width of the [O III] emission line is close to the instrumental profile, with an FWHM measuring 150 km s^{-1}.

high-resolution observations of the cometary globule G287.84-0.82 (Mookerjea et al. 2019), roughly 20 arcmin to the south of η Car. Interestingly, the background [O I] line flux in our observations, 4.0 × 10^{-16} W m^{-2} in the 9.4 arcsec × 9.4 arcsec spaxel, is a factor of 5 above the average measured over a 40 arcmin × 20 arcmin region including the Car I and Car II H II regions (η Car lies just to the SE of Car II) with *ISO*/ long wave spectrometer (LWS; Oberst et al. 2011), taking the spaxel and aperture areas into account.

3.1.3 *H recombination*

Five H I nα lines and one β line are identified, originating from a point-like, centrally located source compared to the PACS PSF (cf. Abraham, Falceta-Gonçalves & Beaklini 2014). An example, from the central spaxel (2,2), is displayed in Fig. 5 comparing the line identified as H I 13-12 (88.795 μm) to the background [O III] (88.36 μm). These far-IR Rydberg states detected in our *Herschel* scans and the H I spectrum in the mid-IR observed with *ISO* are discussed in Sections 3.1.8 and 3.2.4.

3.1.4 *OH 84.5 and 119.3 μm*

Four weak features of rotational doublets of the hydroxyl radical OH at 84.415/84.615 μm and 119.245/119.416 μm have been detected in the central spectrum. After H_2, OH, and CH are the first molecules detected in η Car, through their UV electronic transitions and moving in gas at −513 km s^{-1}, using the *HST*/STIS (Verner et al. 2005b). Detection of the rotational lines is a significant confirmation of this key participant in the creation and regulation of water, which has been reported in *Herschel*/HIFI observations by Morris et al. (2020), and may represent a primary sink of free oxygen in reaction with H_2, i.e. $O + H_2 \rightarrow OH + H$.

3.1.5 *NH_2 152.8/159.8 μm and NH_3 127.1 μm*

In addition to the NH transitions that are discussed below, two weak line complexes of NH_2 (152.80 and 159.75 μm) and one weak line complex of NH_3 (127.11 μm) are detected (see Table 2). Both molecules have *ortho* and *para* spin symmetries whose relative abundances are sensitive to the *ortho*-to-*para* ratio of H_2. This subject is addressed in a more detailed study of the nitrogen hydrides observed at higher spectral and angular resolutions in η Car (Morris et al. in preparation). The NH_3 23.87 GHz inversion line has been detected by Smith et al. (2006). The NH_2 is a first detection in η Car.

3.1.6 *CH_3OH at 69.0 μm*

Emission from CH_3OH 7_4^+–8_5^+ E1 $v_t = 1-0$ is tentatively identified at 69.00 μm. The plausibility of the identification is supported by a preliminary excitation model, including the effects of IR pumping and collisions at a somewhat high molecular density (1 × 10^8 cm^{-3}), and an excitation temperature of 200 K which is adopted in our modeling of the SPIRE spectrum below. The 4346 GHz (68.9805 μm) line of CH_3OH is indeed one of the stronger ones in this part of the far-IR spectrum. While this model is just for guidance and not optimized across more than this isolated line, the model with $\mathcal{N}(CH_3OH) = 1 \times 10^{17}$ cm^{-2} over a line width of 188 km s^{-1} gives an integrated line flux that approximately agrees with the observed line flux (Table 2). A relatively high column density would be expected for a compact source of emission; the ALMA 231.28 GHz feature proposed as CH_3OH 10_2–9_3 A$^-$ $v_t = 0$ by Morris et al. (2020) originates from a compact source, < 2 arcsec in diameter.

3.1.7 *The extended [N II] structure*

The [N II] (121.918 μm) emission from the Homunculus is bright – two to three times above the background levels – and variable with position. From spaxel to spaxel, the flux and the profile wings change considerably. These extensions are associated with the central core plus the outer, fast-moving ejecta that extends from the south-east to north-west, well beyond the Homunculus (Weis, Duschl & Chu 1999; Smith 2008b; Kiminki et al. 2016). The map provides an example of a spatially extended source measured by the 2,2 spaxel to be centred at −49 km s^{-1}, but the FWHM is nearly 700 km s^{-1}, much broader than the PACS spectral response. The centroid velocity shifts to −206 km s^{-1} to the south-east and to +80 km s^{-1} to the north-west, which is significantly larger than the measured instrumental resolution of the PACS (≈150–190 km s^{-1}; see Fig. 6). These quoted velocities ignore possible pointing-induced shifts in the wavelength calibration mentioned above, applying to compact sources.

The [N II] $^2P_{3/2}$–$^2P_{1/2}$ fine structure transition actually consists of six hyperfine components, which collect into three potentially resolvable lines at 121.894, 121.907, and 121.912 μm. With respect to the weighted mean wavelength, 121.898 μm, these have offsets in Doppler velocity of −22, +8, and +36 km s^{-1}, respectively (see Brown et al. 1994). These splittings are significantly smaller than the PACS resolution (at 121 μm, $\Delta v = 150$ km s^{-1}). Thus, the velocity gradients and line widths observed here are dominated by kinematics.

The six brightest spectral profiles extend up to ±800 km s^{-1} on each side of the centroid velocity, indicating large bulk motions of gas to the south-east and the north-west. The general behaviour of the spatial and velocity distributions follow those noted by Currie, Dorland & Kaufer (2002) in their description of the so-called ghost nebula, which was found to be expanding at −500 to +875 km s^{-1} and located exterior to the Homunculus. Additional studies of this outer, rapidly moving structure were done by Kiminki et al. (2016), who measured the proper motion of expanding structures external to the Homunculus. Mehner et al. (2016) used the *VLT*/MUSE instrument to map velocity/spatial structures external to the Homunculus. The resulting three-dimensional model defines the

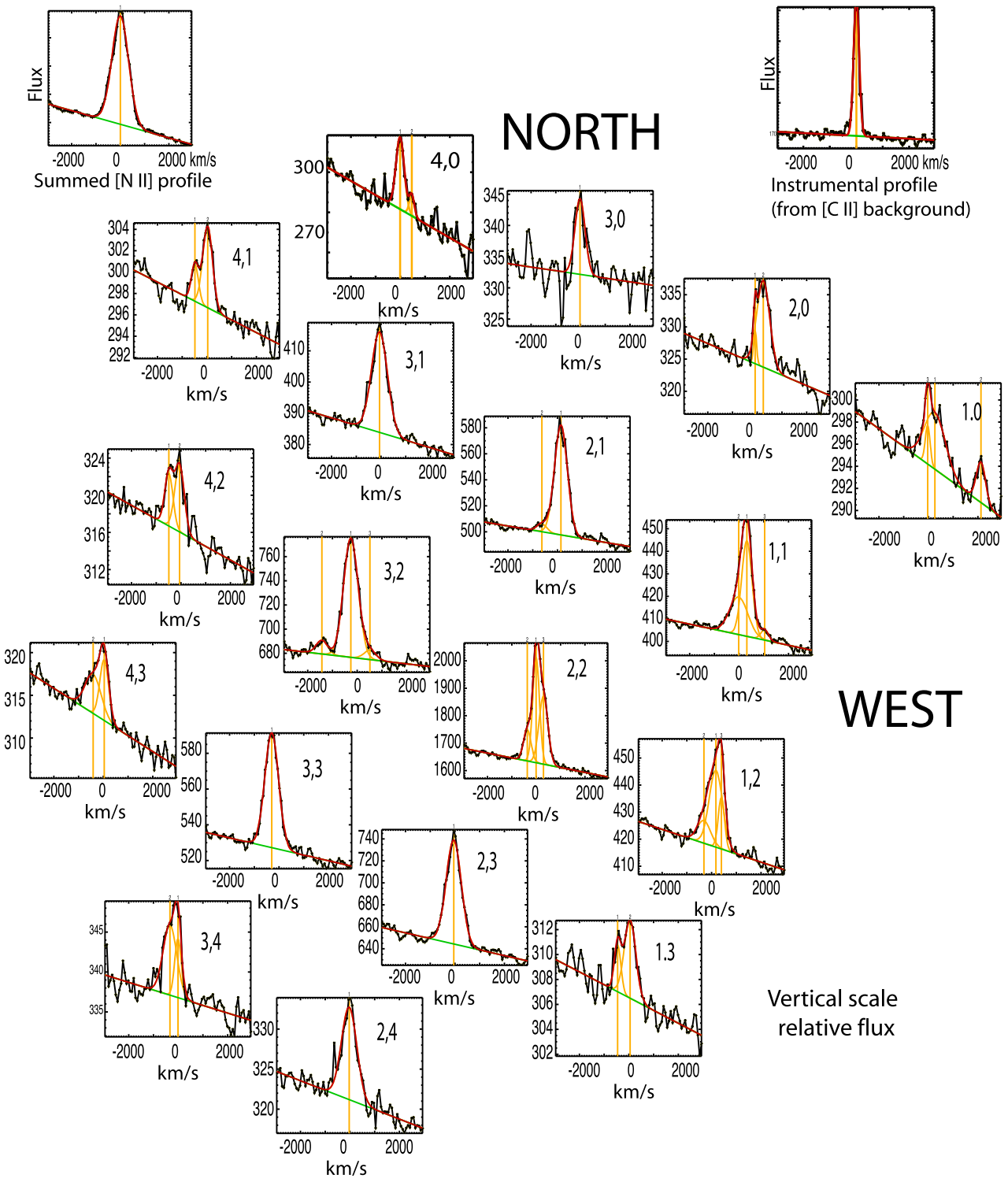

Figure 6. [N II] line profiles on the Homuculus. In the top left corner is shown the [N II] profile summed over the entire PACS array. The top right shows the PACS spectrometer profile of the unresolved background line of [C II] 157.736 μm. The spectral resolution at 121 μm is ∼30 per cent lower. In the centre is shown the mosaic of [N II] velocity profiles. The profiles, labelled with spaxel number, are arranged to reflect the spaxel positions shown in Fig. 2. The summed profile, centred on 3 km s^{-1} has an FWHM of 804 km s^{-1}. However, the peak flux, velocity FWHM, and central velocity change from spaxel to spaxel. Profile variations are consistent with [N II] emission from the Homunculus and the external, fast-moving ejecta.

large outer structure of the very fast moving, numerous 'bullets' external to the Homunculus moving at spatial velocities of several thousand km s^{-1}(Smith 2008a).

3.1.8 The [C II] extended structure

The [C II] (157.736 μm) emission mapping (Fig. 7) exhibits both bright, narrow-line background emission from the Carina Nebula,

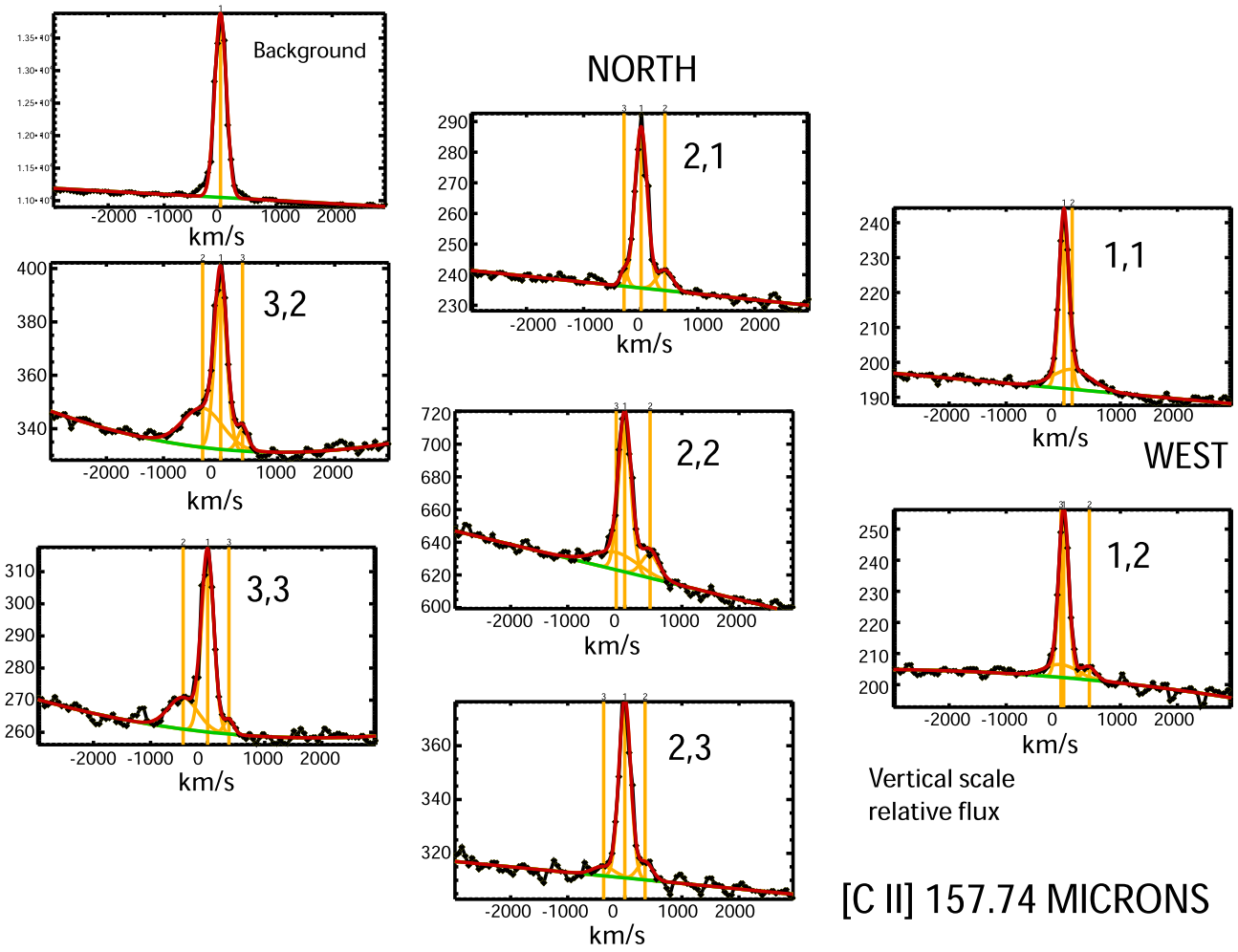

Figure 7. PACS mapping of [C II]. Profiles all have at least two major components: a constant, partially resolved central component and a weaker, broadened component from the Homunculus that follows the large-scale SE to NW velocity shifts of the lobes and equatorial skirt. In some profiles as in (2,2) above, the broad feature is better fit by blue- and red-shifted wings around the central component, consistent with lobe expansion velocities.

and an underlying broad-line, extended emission component from the Homunculus.

The extended narrow-line component is measured to be centred at $v_{\rm LSR} = 0 \pm 10$ km s^{-1} across the PACS array with a nearly constant flux and instrument-limited velocity width. For the central and six adjacent spaxels, weaker, broad-emission components contribute (see Fig. 7, the lower right for this discussion). To the north-west and west, a red-shifted component is present. To the east and south, a blue-shifted component is detected. The [C II] broad component extends over the region of the Homunculus, including the extended skirt structure to the north–north-east (NNE) and to the west–south-west (WSW), but is not external to the Homunculus as is the [N II]. The [C II] emission is not associated with the fast moving ejecta as mapped in [N II] in the visible (Mehner et al. 2016). At spaxel 3,2 (NE of 2,2) and 3,2 (SE), the broad component is shifted to the blue, consistent with material flowing towards the observer. The broad component is approximately centred in velocity in spaxel 2,3 (S) and shifted to the red on the central spaxel (2,2) and 2,1 (N). The broad component shifts to the red for both spaxels 1,1 (NW) and 1,2 (W). These velocities are consistent with the central core at small velocities, the foreground lobe (SE) moving towards the observer and the background lobe receding. The blue-shifted components seen to the east correlate with the forward moving portion of the extended skirt and the red-shifted components seen to the NW and W with a receding portion of the skirt.

Visible/ultraviolet spectral studies of the partially ionized ejecta were accomplished with the *HST*/*STIS*. In line of sight, Nielsen, Gull & Vieira Kober (2005) and Gull, Kober & Nielsen (2006) found multiple shells of partially ionized gas at velocities between −380 and −530 km s^{-1}. The most noticeable shell at −513 km s^{-1} included nearly a thousand NUV absorption lines from singly-ionized iron-peak elements and approximately a similar number of far-UV absorption lines from H_2, along with ground-state absorptions of CH and OH (Verner et al. 2005b). Zethson et al. (2001) and Hartman et al. (2004) discovered the Strontium Filament, located a few arcseconds to the north of η Car in the expanding skirt, which proved to be a metal-ionized intermediate region between the classical H II and neutral, molecular regions. The [C II] emission, given that the ionization potential (I) of neutral carbon is 11.3 eV, below the IP of hydrogen (13.6 eV) and that of nitrogen (14.5 eV) traces the metal-ionized and neutral regions. Hence, molecules might be present in and near the regions of [C II]. Given that the two structures semi-overlap, velocities and positions should be similar.

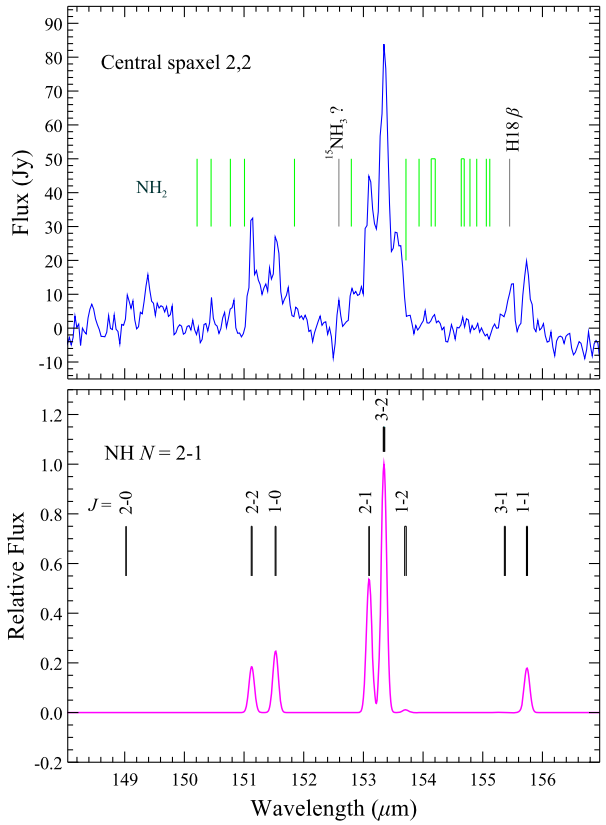

Figure 8. NH $N = 2$–1 complex between 151 and 156 μm. Top: Continuum-subtracted spectrum centred on η Car with vacuum wavelengths shown for H18β, a weak, low significance identification of $^{15}NH_3$, and NH_2 transitions all with upper level energies below 1000 K. The spatial extent of NH coincides with the Homunculus lobes and skirt as demonstrated in Fig. 9. Bottom: A reference non-LTE model of NH over the full range of spin-rotation-hyperfine components, computed at 100 K and zero LSR velocity, convolved with the PACS resolution of 0.05 μm at 150 μm. The width of fiducial lines at each J state indicates the range of hyperfine transitions. Note that three of the eight spin rotation components contribute practically no measurable emission, consistent with their low transition probabilities.

3.1.9 The extended NH structure

The NH $N = 2$–1 transition is absent in the background, but detected by the strongest $J = 3$–2 spin-rotational component at 153.56 μm in the central region (Table 2) and the surrounding Homunculus. This transition is complex, consisting of four spin-rotational components, each with hyperfine structure owing to nuclear-spin interactions with both ^{14}N and ^{1}H nuclei (see Fig. 8).

Three of the spin-rotation components, $J = 1$–2, 2–0, and 3–1, have small line strengths and together contribute less than 0.5 per cent of the total $N = 2$–1 emission. However, significant emission occurs at 153.55 μm in the observed spectrum, which cannot be attributed to either the $J = 1$–2 transition or possible NH_2. This is a strong indicator of more than one velocity component to the NH emission.

Using the same theoretical methods described below in Section 3.2.1 to model the SPIRE spectral survey, we computed synthetic profiles for this NH $N = 2$–1 transition, including including all spin-rotation and hyperfine substates, to provide a clearer picture of the velocity characteristics. The upper level energies of these transitions run from 140.37 to 141.97 K, approximately 92 to 96 K above the lower energy levels. The results are shown in Fig. 9, where we compare synthetic and observed spectra in each spaxel, schematically laid out consistent with the PACS mapping in Fig. 2. Not shown are the flat spectra from the outer spaxels sampling the background Carina Nebula over this range. The fitting has been weighted to the two strongest rotational states $J = 3$–2 and 2–1. Only in the central spaxel do we adopt an interacting continuum of 1200 Jy (integrated thermal emission) based on the extended SED shown by Morris et al. (2017); continuum emission is negligible in the surrounding spaxels.

We find that every spectrum can be well approximated by a two-component model, consisting of a fast component to around ±(400–500) km s^{-1}, and a slower component with v_{LSR} within ±100 km s^{-1}. The slower component generally dominates the emission. While the fitting is weighted on the two strongest J states, the agreement with the weaker lines is qualitatively acceptable, where differences can be attributed to either data quality, or an indication of additional, weaker velocity components. As a test, we added such a third component to the spaxel (2,3) spectrum covering the cap of the SE lobe and backside of the skirt (in projection), which provided marginal improvement in the comparison between observed and total model spectra.

For each model component, the best-fitting LSR velocities, FWHM, excitation temperature, and NH column density are given in the plot legends. Best-fitting temperatures of 50–60 K are derived for the fast moving material, and 150–200 K for the component with $v_{LSR} < 100$ km s^{-1}. Because of the calibration issues in these PACS observations explained in Section 2.1, we stress that the modelling here has been intended mainly to distinguish the principle NH velocities. That said, the total column density for both components in the central spectrum, $N_{2,2}(\mathrm{NH}) = 1.67 \times 10^{15}$ cm^{-2} assuming line widths of 275 and 290 km s^{-1} for the slower and faster components respectively, is only slightly lower than determined from analysis of the SPIRE spectrum (presented below in Section 3.2.1). Summing all spaxels results in excellent agreement.

The velocity structure of NH shown in Fig. 9 presents something of a challenge to interpret. We can immediately exclude detection of NH in the fast outer ejecta or the ghost nebula observed in H Balmer and certain forbidden lines by Currie et al. (2002). Being judiciously wary about potential stray light contamination of the spaxels around the central region, the overall structure of red- and blue-shifted components is none the less consistent with the expanding lobes and skirt as projected by the 45° tilt of the polar axis on to the sky. We are tempted to associate the fast NH with the thin walls of the expanding lobes. The wider spatial extent and 400–500 km s^{-1} velocities would not be inconsistent with an origin of a portion of the NH gas in the equatorial skirt, however, which is more aptly described as break-out material, possibly from more than one of the lesser eruptions that followed the so-called Great Eruption that formed the bipolar lobes. The measured line strengths and column density estimates of the fast component favour association with the bipolar lobes.

Likewise, the slower NH component behaves as expected on the scale of the Homunculus, from approaching to receding in the SW to NE direction, and may point to more wide-scale formation in the Homunculus than, e.g. CO, which is restricted to layers of the dusty central torus over the inner 5–7 arcsec diameter of the structure (see Fig. 1). While the CO profile is asymmetric and broadly flat-topped due to a number of partially overlapping velocity components in the dust rings that make up the disrupted torus (Morris et al. 2017), the total velocity width of the integrated profile is only roughly consistent with the widths of the NH model profiles, 190 km s^{-1} ≤ FWHM ≤ 300 km s^{-1} with corrections for the instrument profile. It is therefore possible that most NH is formed in regions distinct from CO. A summary of our kinematic interpretations of the emission is given in Section 4. High angular resolution observations of NH $N = 1$–0 are needed to further elucidate on the distribution.

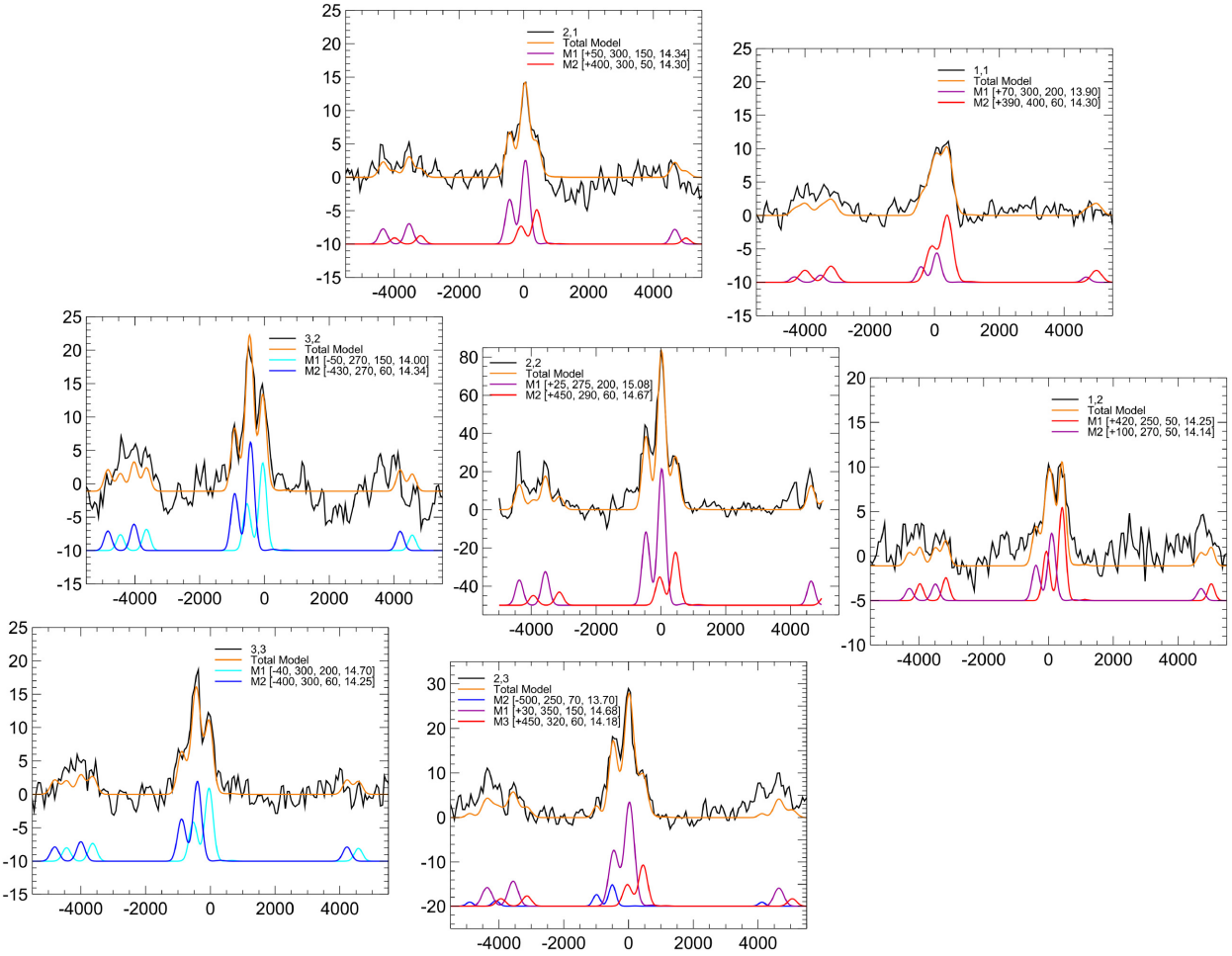

Figure 9. NH $N = 2$–1 profiles observed at seven positions on the Homunculus with synthetic spectra comparisons. Each plot shows LSR velocity in km s^{-1} (referenced to the vacuum wavelength 153.450 μm of the highest transition probability $J = 3$–2, $F_1 = 7/2$–$5/2$ line) versus line flux in Jy and are arranged to correspond schematically to the spaxel positions in Fig. 2. All observed profiles are fitted with two velocity components, except for a three-component model for spaxel (2,3). Total synthetic fits are shown in orange. Individual model components are offset for clarity and coloured to indicate LSR velocity shift ranges of <-100 km s^{-1}(blue), -100 to 0 km s^{-1}(cyan), 0 to $+100$ km s^{-1} (violet), and $>+100$ km s^{-1} (red). For each model component, the LSR velocity (in km s^{-1}), FWHM (km s^{-1}), excitation temperature (K), and log column density (cm^{-2}) are given in the legend. Details on the modelling are given in the text. Features not fitted near -1000 and $+4000$ km s^{-1} are due to NH_2 and H18 β, respectively.

3.2 The SPIRE data analysis

3.2.1 Non-equilibrium models of the molecular line spectra

In order to aid identifications and provide a quantitative analysis of the observed line intensities, we have constructed simple one-zone models of the excitation and line formation for many simple molecules and several atoms and atomic ions. These models treat atomic and molecular processes in some detail, but greatly simplify the radiative transfer. Because the continuum radiation in the infrared is so intense near η Car, the induced radiative processes of absorption and stimulated emission are likely to be important in molecular excitation. As a result, the molecular excitation might depart from LTE. Moreover, the amount of continuum radiation absorbed by different species is greatly influenced by the shielding by dust in complex structures around the central source in relation to the distribution of the gas. This is poorly known except for the few species observed at high angular resolution with *ALMA*, or inferred by velocity-resolved observations with the *Herschel*/HIFI and *APEX* receivers.

We have retained as much detail as possible about atomic and molecular spectra and processes with an enhanced version of the RADEX program to compute non-LTE models of the excitation of a large sample of atoms and molecules. The computed line list is then used to generate a synthetic spectrum, which is finally convolved to the resolution of the SPIRE instrument for comparison with the observed spectrum. The radiative coupling is described with reference to a fixed, empirical model of a passive continuum; that is, the radiative transfer in the lines is not treated self-consistently with the continuum. The RADEX program was described in detail by van der Tak et al. (2007). [NB: The online version and downloadable source code have not yet included the routines for a passive continuum and explicit terms for formation and destruction processes in the rate equations, even though these were present in the equations published by van der Tak et al. (2007).]

To summarize, statistical steady state requires a complete balance among all the rates that populate and de-populate each state i of a molecule. This can be described by a coupled set of rate equations for the state densities n_i subject to the condition that all the densities

are constant in time,

$$\frac{\mathrm{d}n_i}{\mathrm{d}t} = 0 \tag{1}$$

so that loss equals gain for each state i and

$$n_i = \left[D_i + \sum_{j<i} \left(A_{ij} + \bar{J}_\nu B_{ij} + \sum_p n_p q_{ij,p}(T_k) \right) + \sum_{k>i} \left(\bar{J}_\nu B_{ik} + \sum_p n_p q_{ik,p}(T_k) \right) \right] \tag{2}$$

and the right-hand side

$$= F_i + \sum_{m<i} n_m \left(\bar{J}_\nu B_{mi} + \sum_p n_p q_{mi,p}(T_k) \right) \sum_{n>i} n_n \left(A_{ni} + \bar{J}_\nu B_{ni} + \sum_p n_p q_{ni,p}(T_k) \right). \tag{3}$$

This system of equations must be solved simultaneously with the transfer equation so that the internal, integrated, mean intensity $\bar{J}$ can be evaluated. Here,

$$\bar{J}_{nu} = \int_0^\infty J_\nu \phi(\nu)\mathrm{d}\nu / \int_0^\infty \phi(\nu)\mathrm{d}\nu \tag{4}$$

is the profile-weighted integral of the internal intensity integrated over solid angle and averaged over all directions

$$J_\nu = \frac{1}{4\pi} \int I_\nu \mathrm{d}\Omega. \tag{5}$$

In the rate equations, the notation $j < i$ means all states j for which the energy E_j is lower than the energy E_i of the higher state i, and so on. All possible collision partners are denoted by p, and $n_p q_p$ are the number of collisional transitions, downwards for $j < i$ and upwards for $k > i$, per unit volume and time [cm^{-3} s^{-1}]. D_i is the rate [s^{-1}] at which a molecule in state i is destroyed (removed), and F_i is the rate per unit volume [cm^{-3} s^{-1}] at which molecules are formed (added) in state i.

The mean intensity at each transition frequency is obtained through a solution to a transfer equation based on escape probabilities that are averaged over a single uniform emitting zone and over an assumed Gaussian line profile. Morris et al. (2017) modelled the extended infrared/submillimetre source to be a partial annulus 5 arcsec in diameter. For this idealized model, we assumed the thermal continuum source to be distributed in a sphere 5 arcsec in diameter. The mean intensity of the internal continuum at the source is then simply

$$J_\nu^{\mathrm{cont}} = f_\nu / \Omega_s, \tag{6}$$

where f_ν is the observed continuum flux and Ω_s is the solid angle corresponding to an angular diameter of 5 arcsec. The continuum model is shown in two forms in Fig. 10. The lower panel of the figure illustrates that the brightness temperature of the internal continuum is greater than half the photon energy throughout the submillimetre and far-IR part of the spectrum for $\tilde{\nu} < 250$ cm^{-1} (wavelengths greater than 40 μm). The induced radiative transition rates are related to

$$\rho = \frac{A}{\exp(hc\tilde{\nu}/kT_{\mathrm{radiation}}) - 1} \quad \mathrm{s}^{-1}, \tag{7}$$

where A is the spontaneous transition probability, k is Boltzmann's constant, and $T_{\mathrm{radiation}}$ is the brightness temperature at which the Planck function is equal to the mean intensity, $\bar{J} = B_\nu(T_{\mathrm{radiation}})$.

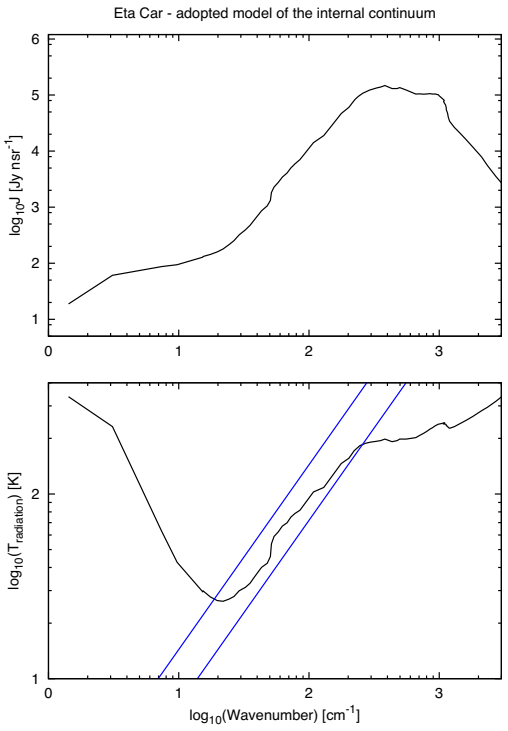

Figure 10. The upper panel shows the internal mean intensity in units of Jy nsr^{-1}. The lower panel shows the same intensity as a Planckian brightness temperature. The straight lines in the lower panel show the photon energy $h\nu/k$ and $h\nu/2k$ in temperature units.

In short, for many common molecules the induced radiative rates in this environment readily compete with inelastic collisions that would otherwise thermalize the excitation, even at densities of the order of 10^8 cm^{-3} or higher.

The enhanced version of RADEX requires both the physical parameters of a model and extensive molecular data files. The basic parameters are the number densities of collision partners (H_2, H, He, e^-, and H^+), the kinetic temperature T_k, and a specification of the continuum radiation. For each atom or molecule, a column density and line width must be specified. Although the formation and destruction rates are formally included, these appear to be important only for the Rydberg transitions of nebular atoms (see Section 3.1.8). For the molecules of the neutral emitting region, nominal values of the formation and destruction rates have been assumed in order to ensure rapid convergence, but these are small enough to have no effect on the computed spectra. With reference to the low-resolution SPIRE spectra, we assume that all species have the same intrinsic line width, 188 km s^{-1} full-width at half-maximum (FWHM), which is large enough to ensure that all of the observed line emission is optically thin. The much higher velocity resolution of *Herschel*/HIFI and ground-based molecular observations reveals complex profiles of lines of CO and other species, with spatially resolved line widths as low as ∼40 km s^{-1}. In the unresolved SPIRE date, the integrated line intensities scale with molecular column density, $\mathcal{N}$, which refers to an average over the assumed size of the source, 5″ in diameter, corresponding to a linear scale of $L = 1.72 \times 10^{17}$ cm based upon the accepted distance, 2.35 kpc (Smith 2006). The result for each molecular transition is an excitation temperature and a line-centre optical depth, from which the line intensity in excess of the continuum

is computed as a function of frequency

$$I_\nu = B_\nu(T_{\rm ex})(1 - \exp(-\tau(\nu)). \quad (8)$$

In the present case, where the optical depths are small, the total spectrum is a simple sum of the contribution of all of the lines. For comparison with the observed spectrum, the computed spectrum is further convolved to the instrumental resolution. The computed spectrum includes both blends of lines of different molecules as well as blends due to unresolved fine- and hyperfine-structure components.

Models were computed for a range of temperatures and hydrogen densities, but with the continuum model fixed. For many of the common molecules with large dipole moments, the radiative coupling is strong enough that the results are not very sensitive to density. The main exception is CO, because its permanent dipole moment is anomalously small and its fundamental vibration occurs at a high enough frequency (>2000 cm^{-1}) that infrared pumping is negligible. There are ten rotational transitions within the ground vibrational state of CO within the frequency range of the SPIRE spectra. Models of CO and CN were used in the first instance to place approximate constraints on density and temperature. It was found that a total density $N(H_2) \approx 10^8$ cm^{-3} at $T_k \approx$ 150–250 K worked rather well.

Note that many of the CO and CN features are actually blends with lines of other species; therefore, the rest of the spectrum was computed at the same time for each of the test cases. The final nominal model adopts a total density of 10^8 cm^{-3} at $T_k = 200$ K. Molecules like HCN, HNC, HCO^+, and N_2H^+ have low-frequency bending vibrations with relatively large transition moments. These species potentially couple strongly to the mid-infrared continuum through their vibrational transitions. Molecular data files were assembled to include such transitions for these molecules. SiO and H_2O have bending vibrations at somewhat higher frequencies, and these were included as well. The model of NH_3 takes into account 847 vibration-rotation-inversion levels with energies up to 4734 cm^{-1} above the ground level and vibration-rotation transition to frequencies up to $\tilde{\nu} \approx 2000$ cm^{-1}. Many of the molecular data files are incomplete in the sense that they lack accurate rate coefficients for inelastic collisions with H_2. In cases where collision rates are missing, rough estimates have been incorporated in order to include at least a crude treatment of the collisional component of excitation.

The chemical formation and destruction terms in equations (2) and (3), F_i and D_i, are constrained so that the total number density of each molecule m is

$$n(\mathrm{m}) = \sum n_i = \sum F_i / D \ cm^{-1} \quad (9)$$

where $D = D_i$ for all i. As proposed by van der Tak et al. (2007), the formation rate is assumed to behave like $F_i \propto \exp(-E_i/kT_{\rm form})$, where E_i is the energy of state i and the formation temperature $T_{\rm form}$ need be merely high enough (∼300 K) to ensure that the relative populations of the nuclear-spin-symmetry species in H_2O, NH_2, and NH_3 approach their high-temperature equilibrium values. The meaning of the column density averaged over the adopted source area in Table 3 is $\mathcal{N}(\mathrm{m}) = n(\mathrm{m})L$ for each molecule, where L is the projected source diameter, 5 arcsec, at the adopted distance. The value of the destruction rate has no noticeable effect on the computed excitation or line intensities as long as $D \leq 10^{-5}$ s^{-1}, which corresponds to destruction of neutral species by reaction with an ion whose fractional abundance is 10^{-4} of hydrogen at a total density $n_{\rm H} \approx 10^8$ cm^{-3}. The exceptional case of CH^+ is mentioned in the following section.

Table 3. Column abundances derived from the SPIRE spectrum.

Molecule	$\mathcal{N}^a$ (cm^{-2})	Vibration[b]
CO	6.1 (17)	Y
^{13}CO	1.5 (17)	N
C I	6.2 (18)	N
HCO^+	1.0 (14)	Y
$H^{13}CO^+$	6.0 (13)	N
CH	3.0 (15)	N
CH^+	7.5 (14)	Y
SiO[c]	<1.0 (14)	Y
H_2O[d]	<1.0 (15)	Y
HCl	5.4 (14)	N
NH	5.0 (15)	N
NH_2	2.5 (15)	N
NH_3	1.0 (15)	Y
N_2H^+	4.2 (14)	Y
CN	1.2 (15)	N
^{13}CN	7.5 (14)	N
HCN	4.0 (14)	Y
$H^{13}CN$	2.5 (14)	N
HNC	2.7 (14)	Y
$HN^{13}C$	1.7 (14)	N

Notes. [a]The column density $\mathcal{N}$ refers to an average over the adopted source area, 5 arcsec in diameter. The notation X (17) means X × 10^{17}.
[b]'Yes' indicates that infrared vibration-rotation transitions are included in the excitation.
[c]Not detected. The derived abundance is an upper limit only.
[d]Transitions are weak and blended, but detected in *Herschel*/HIFI spectra (Morris et al. 2020).

3.2.2 *The molecular model compared to the SPIRE spectrum*

The results of the final model are displayed graphically in a series of seven panels in Fig. 11, showing the computed spectrum overlaid on the observed SPIRE spectrum. This comparison clearly identifies 18 molecular species plus neutral atomic carbon (see Table 3). At least two plausible line blends are needed for a credible identification. The column densities that yield the best match with observed intensities are summarized in Table 3.

The tabulated column densities reveal the relative abundances over the complete chemical network of species observed in the SPIRE spectrum. The agreement in CO, ^{13}CO, CN, HCN, $H^{13}CN$, HCO^+, HNC, and N_2H^+ relative abundances with previous studies of these species observed with single dish heterodyne receivers (Loinard et al. 2012; Morris et al. 2017) is very good. We note that the column densities tabulated by Loinard et al. (2012) are more than an order of magnitude higher than our results and those of Morris et al. (2017) for CO and ^{13}CO. However, this is mainly due to an assumed small source size of 1 arcsec diameter, and secondarily to the exclusion of continuum interactions in the analysis by Loinard et al. (2012). CO shares a very similar velocity structure with the other molecules quoted here, and is distributed in the extended torus-like structure (see Fig. 1), which we more reasonably approximate as a 5 arcsec diameter sphere. Taking these differences into account, our tabulated abundances are only slightly higher in those species by factors of 1.2–2.8, affording us to take confidence in chemical abundances to at least their tabulated orders of magnitude.

The ratios of ^{12}C and ^{13}C isotopologues require a separate, more careful assessment. The dominant ^{12}C forms of several molecules include effects of infrared pumping through vibrational transitions; however, the minor forms of the same molecules lack the extensive data files. As a result, the column densities of the minor isotopologues

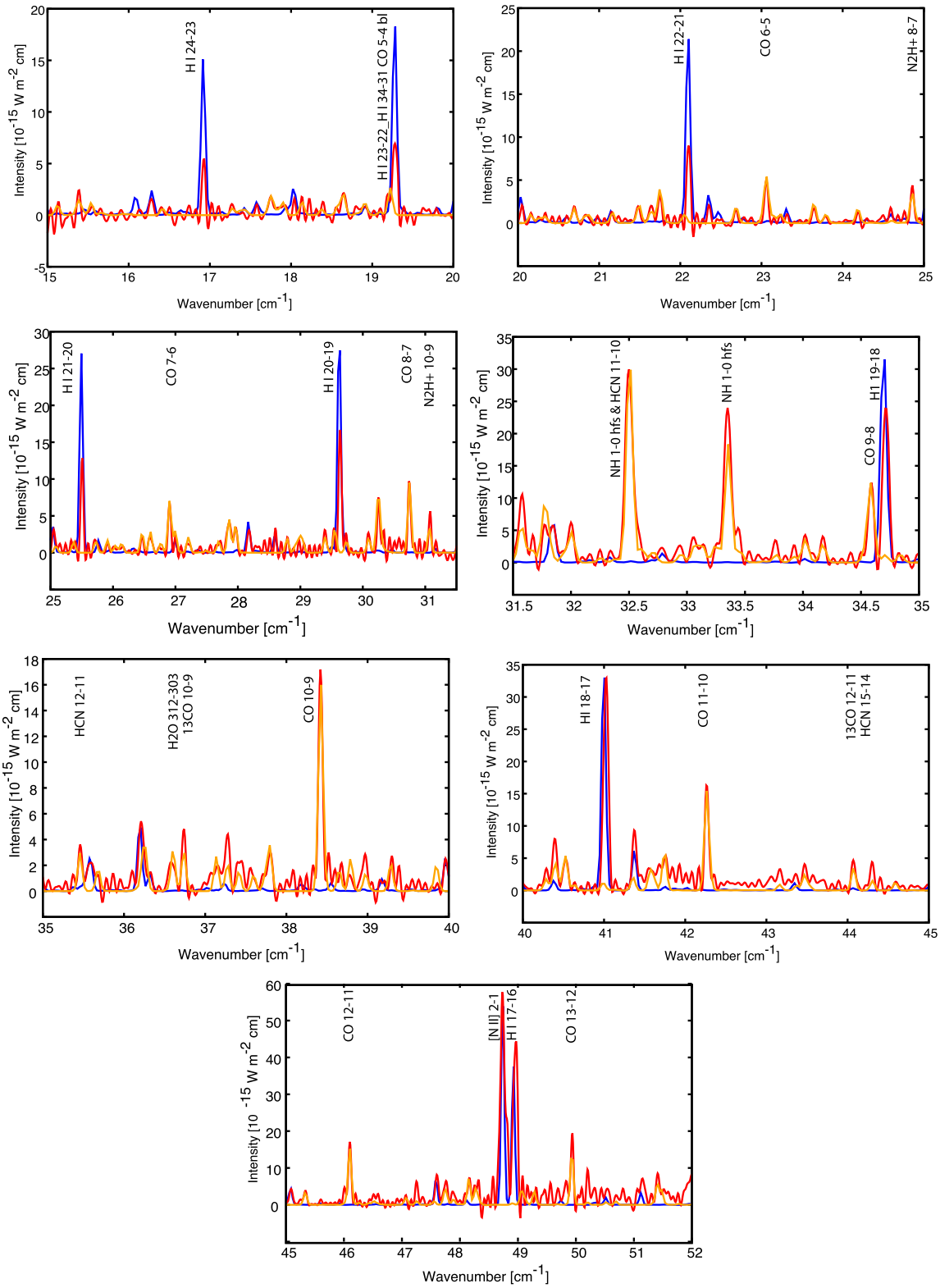

Figure 11. Model fits to the SPIRE spectrum each subpanel includes the actual spectrum (red), the fit to the atomic recombination (blue) and the fit to the molecular spectrum (orange). A number of brighter emission features are identified, but with this low spectral resolution, blends are abundant. Preliminary line identifications are listed in Tables A1–A4 and in more detailed plots in Figs A1–A13.

might be somewhat overestimated, and the corresponding $^{12}C/^{13}C$ abundance ratios underestimated. This effect is probably not severe for CO, suggesting that the isotope ratio might be consistent with a value of approximately 4. Independent analysis by Morris et al. (2017) of the CO ladder observed at high spectral resolution with HIFI and *APEX* suggests an even lower value of $[^{12}C/^{13}C] \approx 3$.

The entry for H_2O in Table 3 is very uncertain. Although several possible rotational lines of water occur over the SPIRE spectral range (Figs A1–A13) and line list (Table A1), only one of these, the *ortho*-H_2O $3_{12} - 3_{03}$ line at 36.604 cm^{-1} (1097.36 GHz), is free of blending with a strong line of a different but otherwise well-identified species. None the less, H_2O lines have been convincingly detected with HIFI by Morris et al. (2020) at 18.58 cm^{-1} (556.94 GHz) and 32.96 (987.93 GHz), which are the *ortho* and *para* transitions $1_{1,0}$–$1_{0,1}$ and $2_{0,2}$–$1_{1,1}$, respectively. They estimated column densities in the range of 2.5–5.0 $\times$ 10^{13} cm^{-2}, which is about a factor of 20–40 lower than the upper limit set by our model of the SPIRE data. Similarly, SiO has been included in the model, but is not detected in our *Herschel* spectra or reported in ground-based observations.

The highly reactive molecular ion CH^+ is exceptional. CH^+ is destroyed on nearly every collision with the most abundant collision partners (H, H_2, electrons), so that 'chemical pumping' can compete with inelastic collisions in its rotational excitation. CH^+ also couples very strongly to the intense far-infrared radiation field in eta Car. Accordingly, CH^+ excitation was treated with higher formation and destruction rates than the other molecules. Even with these complications, the models show that when $D(CH^+)$ is changed from 0.1 to 10^{-6} s^{-1}, the calculated intensities of the two lowest rotational transitions change by less than 30 per cent. Only the $J = 1$–0 line is covered in the SPIRE passband, thus the entry for CH^+ in Table 3 is based upon a single transition.

Unfortunately, there is no simple way to estimate the total hydrogen column density for the same neutral emitting zone that produces most of the molecular line emissions in the SPIRE spectrum. The elemental abundances in the ejecta of η Car are known to be unusual compared with abundances in the interstellar medium. Both the overabundance of nitrogen and the low ratio of $^{12}C/^{13}C$ reinforce the fact that the ejecta is heavily-processed material from a massive star. We will return to the abundances in (Section 4).

3.2.3 *Modeling the hydrogen Rydberg transitions*

The SPIRE spectrum of η Car is dominated by strong lines of atomic hydrogen, arising in Rydberg states with principal quantum number $n \geq 16$. These lines most likely arise in photo-ionized nebular gas close to the star or in an ionized wind. Recent *ALMA* observations of Rydberg transitions at longer mm wavelengths suggest that the line emission is concentrated on subarcsecond angular scales (Abraham et al. 2014). Astronomical Rydberg transitions are commonly referred to as recombination lines, because the high-n levels in dilute nebulae are populated initially by the process of radiative recombination

$$H^+ + e^- \rightarrow H(n) + \gamma$$

followed by a radiative cascade $n \rightarrow n''$, with additional redistribution by inelastic collisions with electrons and protons. In the dense, ionized wind of an LBV like η Car, it is possible that some of the excitation derives directly from electron-impact out of the lowest levels of the neutral atom, in which case it is not strictly appropriate to call the observed transitions recombination lines.

The atomic lines in the SPIRE spectrum are unresolved, and the projected entrance aperture is much larger than the extent of the dense nebula and/or ionized wind. Unlike a typical idealized nebula, the ionized gas around η Car is exposed to an extremely intense radiation field at far-infrared and submillimetre wavelengths. Absorption and stimulated emission in this radiation may contribute significantly to the excitation of the observed Rydberg states in H and He. At the same time, a realistic model must account for the intensities of the lines that are observed in excess of a strong continuum. It is beyond the scope of the present analysis to perform a fully self-consistent model of the ionized gas. Instead, we treat the atomic lines similarly to the molecular lines, striving first of all to assess the competition among the processes of radiative capture and cascade, inelastic collisions with electrons, and radiative pumping under nebular conditions. We apply the same expanded version of the RADEX code discussed above for molecules in order to compute single-zone, non-LTE models of the excitation and line spectra of H I, He I, and He II. Atomic data files contain levels $n = 1$–500 with all allowed radiative transitions and inelastic e-impact rate coefficients similar to those adopted by Hummer & Storey (1987). The rate of formation of each initial state n_i is computed as

$$F(n_i) = \alpha_{n_i}(T_e) N(e) N(\mathrm{ion}) \quad cm^{-3}\ s^{-1}\,, \tag{10}$$

where $\alpha_{n_i}(T_e)$ is the rate coefficient of radiative recombination into level n_i at electron temperature T_e, computed through use of computer routines published by Flower & Seaton (1969). Number densities of electrons, $N(e)$, and the recombining ion, N(ion), are given upper-case symbols here to distinguish from the principal quantum number n.

The reference model is a uniform sphere of hydrogen, helium, and electrons that is assumed to subtend an angular diameter of 0.5 arcsec. The corresponding path-length is $L = 1.72 \times 10^{16}$ cm at the distance of η Car. The adopted He/H abundance ratio is 0.08 by number of nuclei. Owing to the strong effect of radiative pumping on Rydberg states $n = 15$–30, the spectrum is not expected to be sensitive to temperature; therefore, we simply assume $T_e = 8000$ K.

For guidance on the neutral fractions and formation rates inside the nebula, we take a very simple model of a static photo-ionized nebula illuminated by the ultraviolet light of a 37 500 K blackbody with a bolometric luminosity of 10^6 $L_\odot$. This is a poor representation of the marvellous complexity of η Car, whose true ultraviolet spectrum is completely hidden from us. The diameter of the corresponding Strömgren sphere is set equal to the adopted path-length L. Under these assumptions, the total density of hydrogen is $N_H = 7.6 \times 10^6$ cm^{-3}, and the column density of neutral H within the ionized zone is $\mathcal{N}(\mathrm{H}) = 3.6 \times 10^{18}$ cm^{-2}. These numbers set the conditions for the RADEX models of the H I spectrum, notably the total rates of formation (equation 10) and destruction of neutral H within the nebular zone. The same model of the continuum spectrum adopted for the molecular excitation is applied here. That spectrum was computed from the observed SED averaged over an adopted source diameter of 5.0 arcsec.

The distributions of He, He^+, and He^{++} within the ionized zone are sensitive to the detailed shape of the input ionizing spectrum. In the reference model in one dimension, helium is singly ionized out to 93 per cent of the ionized-hydrogen radius, and doubly ionized only to 8.25 per cent of the radius. The predicted He II spectrum from the recombination of He^{++} is useful not as a quantitative prediction but only for the sake of constructing a finding list of possible lines.

Even though the reference model of the ionized gas is simplistic, it shows that nebular gas of the indicated density, temperature, and extent can provide H I lines with intensities of the right order

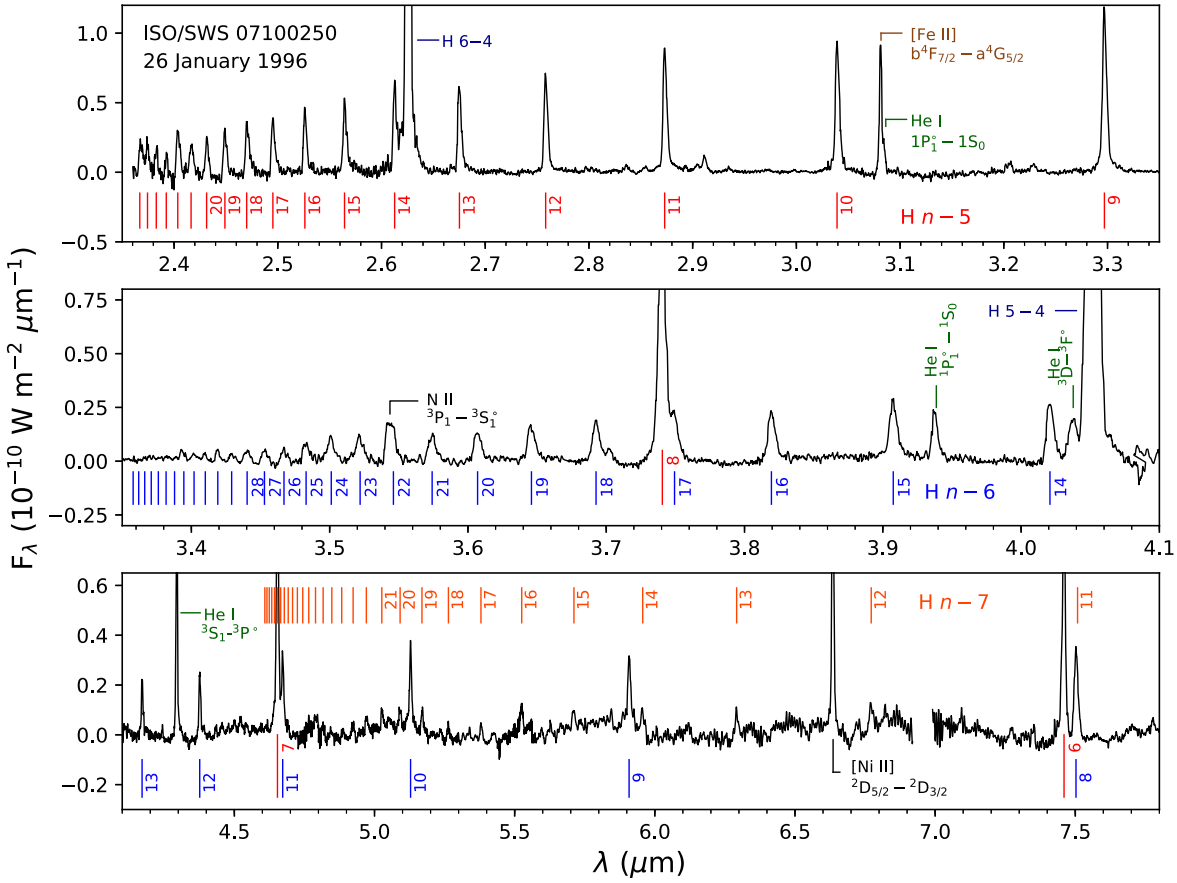

Figure 12. The continuum-subtracted *ISO*/SWS spectrum of η Car over the first 5 grating subbands of the S01 spectral scan obtained in 1996. The continuum rises from 2.5×10^{-10} to 6.2×10^{-10} W m^{-2} μm^{-1} (500–2050 Jy) over this range. The H I lower quantum state $n_l = 5$ (Pfund), 6 (Humphreys), and 7 series are indicated, along with the Brackett α (5–4) line and identifications for leading lines of other atomic species. The spectral resolution R = 1500–2000, or 200 km s^{-1} at 3.0 μm.

of magnitude. Moreover, the simple model allows us to assess quantitatively the atomic processes that control the line emission in the environment of η Car. In the model, the Rydberg states of H with $n \geq 20$ follow rather closely a Boltzmann distribution but at a temperature $T_e^{'} = 3855$ K that is rather smaller than the kinetic temperature. At lower n, the populations are inverted. As a result, the lowest α lines ($\Delta n = 1$) in the SPIRE spectrum, H 16α and 17α, are weak masers with optical depths $\tau > -0.1$, while H 18α through 22α have suprathermal excitation temperatures in the range T_{ex} = 10 000 to 40 000 K. These features of the model are mainly due to the strong coupling to the continuum radiation in the far-infrared. The synthetic spectrum of the reference model is displayed as red in Fig. 11. In Section 3.2.4, we will apply our modelling to the mid-infrared H lines observed with *ISO* to examine the non-LTE effects of the coupling.

The frequency interval 400–1600 GHz contains 2478 lines of H I, He I, and He II with line-centre optical depths $\tau > 10^{-4}$. The peak intensities of lines in the model agree well with the observations at the lower frequencies, but at $\tilde{\nu} > 25$ cm^{-1} ($\lambda < 400$ μm), the α lines $\Delta n = 1$ are approximately 1/2 as strong as observed, while the weaker, higher order β and γ lines ($\Delta n = 2$, 3) are somewhat closer to the observations. The intensities of the α transitions are most sensitive to the non-LTE effects at SPIRE frequencies. These effects are thought to be closely tied to the balance between density-dependent recombination and collisional excitation on the one hand and radiative pumping in the ambient continuum on the other hand. As a result, no attempt has been made to fine-tune the model parameters to achieve a better fit.

Even though the He I lines are ∼0.1 times as strong as the corresponding H I lines, it is important to include them, because they shift centroids of the unresolved blends into better agreement with the peak positions in the observed spectrum.

The intensity of [N II] line at $\tilde{\nu} = 48.738$ cm^{-1} (1461 GHz) requires a column density of ionized nitrogen $\mathcal{N}(N^+) = 3.14 \times 10^{21}$ cm^{-2} in the nebular model, corresponding to an abundance ratio $N^+/H^+ = 0.024$ in the ionized gas.

Finally, the total mass of gas (hydrogen and helium) in the ionized region is only 0.022 $M_\odot$, trivial in comparison with the mass estimated for the neutral and dusty ejecta of η Car.

3.2.4 A new analysis of the mid-infrared H I line spectrum

An immediate and lasting impression of η Car's infrared SED is the enormous amount of thermal energy produced by heated dust grains, peaking in flux density at 70 000 Jy near 25 μm (see fig. 7 in Morris et al. 2017). Despite the steeply rising continuum in the 2–25 μm range, a rich spectrum of H I lines from the ionized gas of the wind and surrounding nebula is observed at high S/N in the *ISO*/SWS spectrum, from the instrument's lower wavelength cut-off of 2.4 μm to around 9 μm. The continuum-subtracted spectrum is shown in Fig. 12. An analysis of these lines complements the

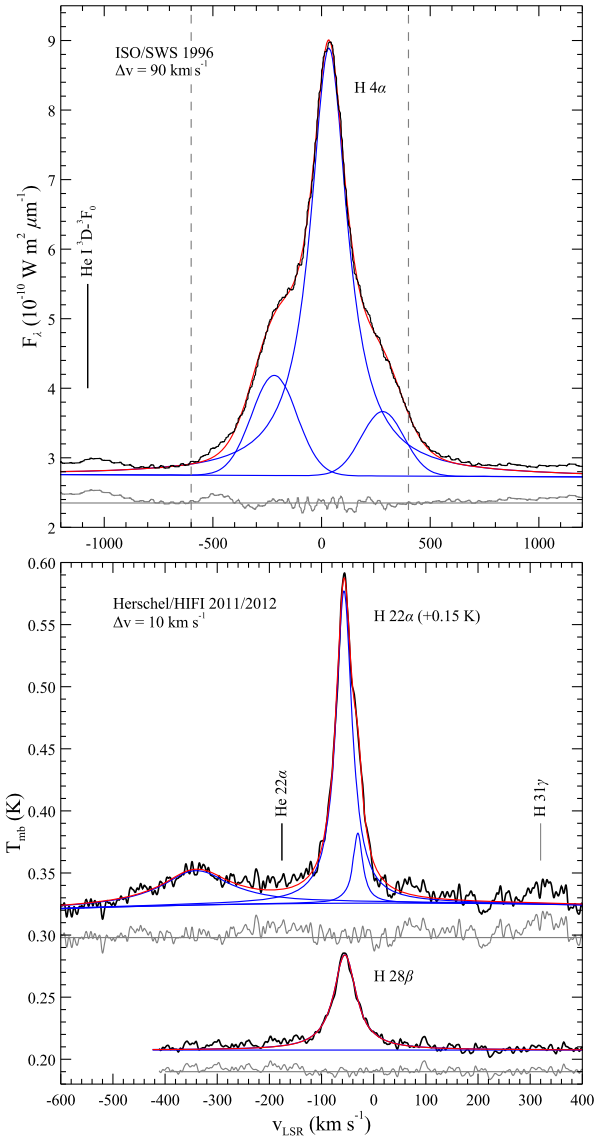

Figure 13. *ISO*/SWS and *Herschel*/HIFI observations of H I α lines. The SWS spectrum of Br α (top) was obtained in the highest grating resolution mode for line scanning, at $R = 3500$. Vertical dashed grey lines indicate the plotted range of the H22 α line shown in the lower panel, to emphasize the difference in profile widths. The broad, weak feature near -350 km s^{-1} in the lower plot is unidentified.

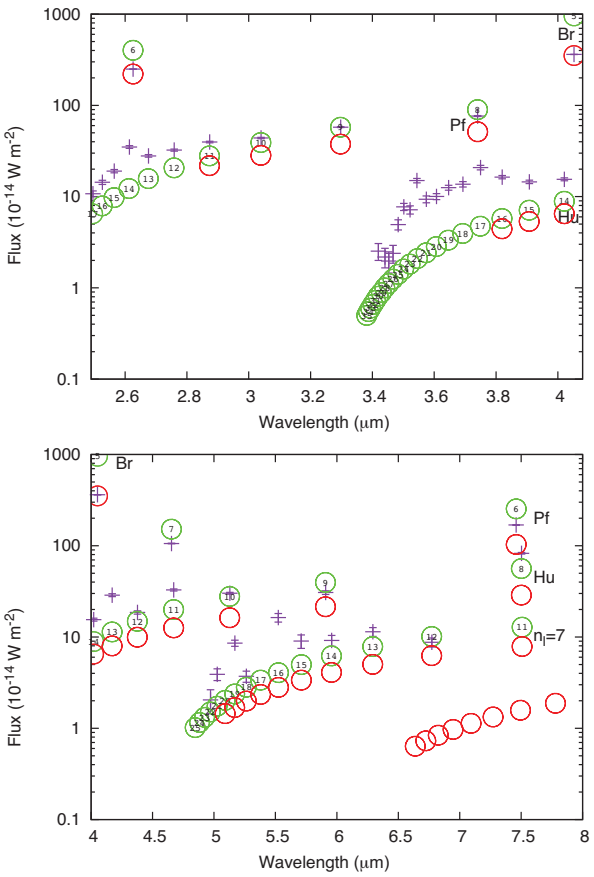

Figure 14. Excitation diagram for the mid-infrared hydrogen lines observed with *ISO*/SWS. The integrated fluxes of the H I Br, Pf, Hu, and $n_l = 7$ series are shown as violet crosses as a function of wavelength. The upper-state quantum numbers are indicated inside the green circles, which show fluxes expected in LTE at $T_e = 10^4$ K when reddened by an interstellar extinction curve with $A_V = 5$ mag. The red circles show the predicted fluxes of the non-LTE capture-cascade model used to analyse the far-infrared *Herschel* spectra.

preceding interpretation of the far-IR Rydberg transitions, providing insight into the role of the strong continuum on the spectral energy budget of these lines over more than a factor of 100 in wavelength.

All of the lines identified in this part of the spectrum can be attributed to the ionized gas of the wind or compact nebula, not necessarily at the same velocities. This is nicely illustrated in higher spectral resolution observations of several H I α transitions, shown in Fig. 13 where the SWS spectrum of H Br α was obtained in the line scan (S02) mode at 90 km s^{-1} resolution, and the HIFI spectrum of the submillimetre H22 α line is shown with $\approx$10 km s^{-1} smoothed resolution. The HIFI Rydberg lines are weakly structured and quite narrow compared to the Br α line, which is composed of a central core, best fit by a Lorentz profile with a FWHM of 180 km s^{-1} (corrected for the SWS instrument profile), and extended wings of emission to which we have fit Gaussian profiles centred near -220 and $+280$ km s^{-1}. If there is any mid-infrared H I emission from the gas component that gives rise to the submillimetre line emission at $v_{\rm LSR} = -50$ km s^{-1}, it is completely buried in the large beam of the SWS, and too weak to influence the profile fitting. This conclusion is consistent with our model calculations, discussed below.

The continuum subtraction in the SWS spectrum at $\lambda > 4.5$ μm is affected by the presence of broad dust bands, leading to a somewhat choppy residual baseline in the lower panel of Fig. 12; however there are no gas-phase molecular lines evident in the SWS spectrum. For example, vibration-rotation first overtone and fundamental lines of CO at 2.3 and 4.6 μm, NH_2 near 6.7 μm, and NH_3 near 10 μm (out of the plotted range) might be expected, although the detectability of such lines would depend both on the excitation temperatures relative to the continuum brightness, on the fraction of the continuum covered by the molecular gas, and on the instrumental resolution. The non-LTE molecular model of the *Herschel* spectra can be used to predict the mid-infrared spectrum: no lines are predicted to be detectable against the intense continuum at the resolution of the SWS spectra.

The rich mid-IR H I spectrum complements the interpretation of the far-IR Rydberg transitions, as illustrated in Fig. 14 giving a view on excitation in which the measured line fluxes (listed in Table 4) are displayed as violet crosses with statistical error bars versus

Table 4. Measured *ISO*/SWS 2.4−8.8 μm line fluxes[a].

Observed (μm)	Vacuum (μm)	Line Flux (10^{-14} W m^{-2})	n_l	n_u	Identification
2.49577 (0.00008)	2.49526	10.77 (0.79)	5	17	H I unless indicated
2.52643 (0.00006)	2.52610	14.36 (0.75)	5	16	
2.56477 (0.00006)	2.56433	19.04 (0.79)	5	15	
2.61397 (0.00008)	2.61266	35.01 (1.19)	5	14	
2.62580 (0.00001)	2.62588	250.14 (0.94)	4	6	
2.67551 (0.00005)	2.67514	27.95 (0.91)	5	13	
2.75864 (0.00004)	2.75828	32.37 (0.86)	5	12	
2.87344 (0.00003)	2.87300	39.65 (0.79)	5	11	
2.91110 (0.00030)	2.91144	6.12 (0.89)	.....	.....	[Ni II] $^4F_{5/2} - {}^2F_{7/2}$
3.03961 (0.00003)	3.03921	43.93 (0.75)	5	10	
3.08159 (0.00003)	3.08095	28.00 (0.61)	.....	.....	[Fe II] $b^4F_{7/2} - a^2G_{5/2}$
3.29728 (0.00002)	3.29700	57.71 (0.63)	5	9	
3.41937 (0.00031)	3.41911	2.53 (0.53)	6	30	
3.44072 (0.00034)	3.44032	2.18 (0.53)	6	28	
3.45309 (0.00034)	3.45286	1.97 (0.51)	6	27	
3.46701 (0.00033)	3.46698	2.39 (0.53)	6	26	
3.48349 (0.00027)	3.48297	4.94 (0.63)	6	25	
3.50163 (0.00023)	3.50117	7.73 (0.69)	6	24	
3.52203 (0.00023)	3.52203	7.18 (0.74)	6	23	
3.54403 (0.00014)	3.54611	14.99 (0.82)	6	22	+ N II $^3P_1 - {}^3S^\circ_1$
3.57467 (0.00022)	3.57411	9.35 (0.81)	6	21	
3.60744 (0.00018)	3.60698	10.03 (0.77)	6	20	
3.64639 (0.00016)	3.64593	12.55 (0.78)	6	19	
3.69277 (0.00018)	3.69264	13.68 (0.92)	6	18	
3.74046 (0.00004)	3.74057	76.39 (0.95)	5	8	
3.74976 (0.00021)	3.74940	20.81 (1.17)	6	17	
3.81991 (0.00010)	3.81946	16.36 (0.69)	6	16	
3.90783 (0.00009)	3.90756	14.51 (0.62)	6	15	
4.02111 (0.00008)	4.02088	15.49 (0.57)	6	14	
4.04313 (0.00026)	4.04429	25.71 (1.29)	.....	.....	He I $^3D - {}^3F^\circ$ triplet
4.05211 (0.00000)	4.05228	361.88 (0.68)	4	5	
4.17157 (0.00013)	4.17080	28.72 (1.06)	6	13	
4.29471 (0.00002)	4.29596	72.61 (0.80)	.....	.....	He I $^3S_1 - {}^3P^\circ$
4.37693 (0.00009)	4.37646	18.58 (0.76)	6	12	
4.65386 (0.00002)	4.65379	105.82 (0.79)	5	7	
4.67250 (0.00009)	4.67252	32.79 (0.87)	6	11	
4.97177 (0.00053)	4.97089	2.05 (0.60)	7	22	
5.02635 (0.00032)	5.02610	3.91 (0.57)	7	21	
5.12883 (0.00007)	5.12867	30.16 (0.66)	6	10	
5.17013 (0.00024)	5.16929	8.58 (0.66)	7	19	
5.26336 (0.00028)	5.26369	3.71 (0.52)	7	18	
5.52351 (0.00054)	5.52520	16.32 (1.77)	7	16	
5.70929 (0.00072)	5.71147	9.02 (1.52)	7	15	
5.90880 (0.00019)	5.90823	30.71 (1.40)	6	9	
5.95737 (0.00046)	5.95685	9.17 (1.24)	7	14	
6.29316 (0.00048)	6.29193	11.42 (1.26)	7	13	
6.63551 (0.00004)	6.63596	87.70 (0.99)	.....	.....	[Ni II] $^2D_{5/2} - {}^2D_{3/2}$
6.77325 (0.00040)	6.77200	8.76 (0.99)	7	12	
7.45930 (0.00004)	7.45988	168.75 (1.48)	5	6	
7.50340 (0.00010)	7.50251	82.69 (1.59)	6	8	blend 7.50812 H I 7 − 11
8.76050 (0.00063)	8.76008	12.45 (3.69)	7	10	

[a]Values in parentheses are statistical (formal) measurement uncertainties. The wavelength calibration of the SWS grating is accurate to $\lambda/\delta\lambda \sim 10000$, or 0.0003 μm at 3.0 μm Valentijn et al. (1996). Relative line intensity calibration errors are less than 3 per cent from 2.4 to 4.1 μm, and around 5 per cent over 4.1–8.8 μm.

wavelength of the transition. The green circles indicate the intensities expected in LTE at a temperature $T_e = 10^4$ K and reddened by $A_V =$ 5 mag of visual extinction using a standard Galactic extinction law (e.g. Indebetouw et al. 2005). The numeral inside each green circle is the principal quantum number of the upper state n_u of the transition. The red circles indicate the intensities predicted by the same *non-LTE* model that was applied to the SPIRE spectra, but scaled to the observed flux of the H Br α (5–4) line at 4.08 μm.

The key result of Fig. 14 is that the lines of the H I Pf, Hu, and $n_l = 7$ series show significant deviations from LTE intensities for upper-state quantum numbers n_u in the range 13 through 25. This is the same range of quantum numbers sampled by the α lines,

$\Delta n = 1$, in the SPIRE and PACS spectra. These deviations can be attributed to the radiative pumping of these Rydberg states by the intense continuum radiation of η Car. The magnitude of these effects is quite sensitive to the details of the radiative transfer, which our single-zone escape-probability model does not completely represent, and deserves follow-up. The model does, however, reveal that the α and β transitions with $n_u \approx 13$–25 have inverted populations and negative excitation temperatures. The maser amplification factors in the nominal model are close to unity.

4 SUMMARY AND CONCLUSIONS

4.1 η Car's molecular inventory

A critical view generally held prior to the launch of *ISO* of η Car lacking the conditions to support a significant observable component of molecular gas other than H_2 is transformed almost immediately by the rich PACS and SPIRE spectral scans presented in this paper, as well as subsequent ground-based observations acquired during the analysis and in follow-up to our *ISO* programme. Indeed, while the detected lines span tens to hundreds of km s^{-1} in width and are relatively weak over the thermal continuum particularly at $\lambda < 300$ μm, the inventory of molecules detected in η Car stands now at 20, including the 18 molecules listed in Table 3 (i.e. excluding SiO which is not detected), H_2 (Smith 2002), and possibly CH_3OH (Morris et al. 2020). Of the species tabulated here, about half have previously been reported through transitions accessible from the ground in the submillimetre range (CO, ^{13}CO, CN, HCN, H^{13}CN, HCO$^+$, HNC, and N_2H^+ by Loinard et al. 2012) and in the UV from space with *HST*/STIS (CH and OH by Verner et al. 2005b). Unambiguous detections of H_2O and NH with *Herschel*/HIFI, and identification of a feature in *ALMA* observations and supporting weaker features in HIFI spectra as CH_3OH have been published as part of our *Herschel* programme (Morris et al. 2020).

Our observational results also remove ambiguity about NH_3 in the Homunculus, based on an identification of the $J_K = 3_3$ inversion line at 23.87 GHz by Smith (2006) but challenged by Loinard et al. (2016) to be associated instead with the H81 β recombination line. The observations by Smith (2006) show that the line emission has a different velocity structure and is more extended than we would expect from H recombination as observed with *ALMA* (cf. Abraham et al. 2014). Regardless, the NH_3 rotational transitions detected in our *Herschel* spectra (including HIFI, which will be published elsewhere) confirm this molecule along with nitrogen-bearing NH, NH_2, N_2H^+, CN, HCN, HNC, and ^{13}C isotopologues for the C-bearing nitrides.

4.2 Distribution of the atomic and molecular gas

The PACS and SPIRE spectral scans are rich in lines; however, at the angular resolutions of both instruments compared to the 10 arcsec × 18 arcsec nebula, we can surmise the locations where the bulk of the far-IR line emission originates only on the scales of the physical structures described in the Introduction section and Fig. 1. Our current understanding of the distribution of the atomic and molecular species detected in these observations is illustrated in Fig. 15, and summarized as follows:

(i) The continuum is unresolved with PACS in 9.4 arcsec × 9.4 arcsec spaxels over the full usable wavelength range for the spectrum, 55–190 μm. In the SPIRE observations, Morris et al. (2017) has shown that the continuum at 305 μm is within a diameter 2–5 arcsec across, based on a semi-extended source size analysis

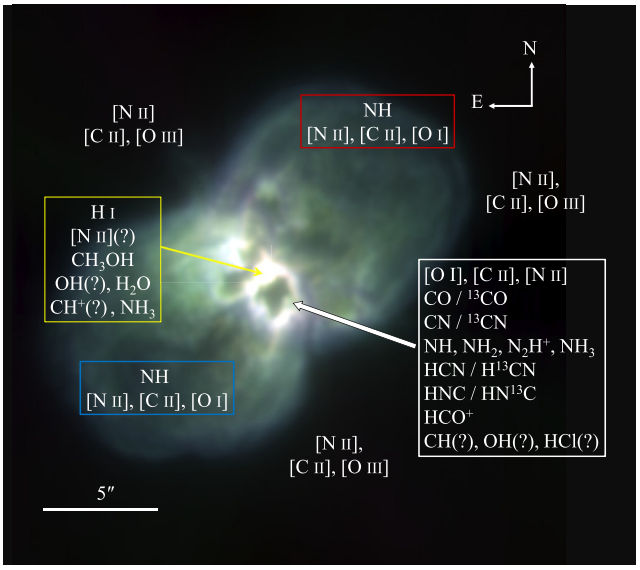

Figure 15. A false colour mid-infrared 9.0 μm image of η Car with bulk locations of the atomic and molecular species detected in the PACS and SPIRE spectral survey as summarized in Section 4. The colour scheme provides a good association of the white high contrast emission defining the Butterfly Nebula and species in the white box. Species surmised to originate within 1 arcsec of the central source (i.e. 2 arcsec across) are indicated in the yellow box. The red and blue boxes contain molecules associated with the expanding lobes (or break-out material of the equatorial skirt). Detected background species are indicated without boxes. The image was taken with the VLT/VISIR instrument through the [Ar III] filter (Mehner et al. 2019), sampling the $T \geq 400$ K continuum.

where the short wave and long wave sections overlap at different beam sizes.

(ii) Hydrogen recombination and most atomic lines likewise appear to originate from a compact source well within the 10 arcsec diameter region centred on η Car. Based upon the radio observations of Duncan & White (2003) and *ALMA* observations by Abraham et al. (2014), the bulk of the hydrogen recombination lines originate from within 0.″5 of η Car.

(iii) The [N II] emission, while centred on η Car is extended from the SE (blue-shifted) to the NE (red-shifted). While the bulk of the [N II] emission originates from the central region, a fainter component maps to the spatial extent (40–50 arcsec) of the fast-moving bullets described by Weis et al. (1997), Smith (2008b), and Kiminki et al. (2016).

(iv) NH on the other hand is not detected in the fast outer ejecta or the ghost nebula observed in H Balmer and certain forbidden lines. The overall structure of red- and blue-shifted components is consistent with emission in the expanding lobes and break-out material from the skirt. The fast NH may be from the thin walls of the lobes, favoured by the measured line strengths and estimated column densities. Similarly, the slower NH component behaves as expected on the scale of the Homunculus, from approaching to receding in the SW to NE direction, and may point to more wide-scale formation in the Homunculus than, e.g. CO, which is restricted to layers of the dusty central torus over the inner 5–8 arcsec diameter of the structure.

(v) The [O III] emission originates entirely in the background Carina Nebula and is relatively constant over the PACS spaxels with the exception of a relative minimum centred on η Car. This may be due to the fossil winds having driven out nebular material and having replaced it with nitrogen-enriched processed material. We

have detected [O I] on the central source, where it is resolved and surprisingly structured with at least four velocity peaks.

(vi) The [C II] emission is primarily background emission from the Carina Nebula, but a broad component correlates with the spatial structure of the Homunculus and the broad component shifts to the red and blue as would be expected for various components of the expanding Homunculus bipolar lobe and skirt. [C I] 492 GHz is only weakly detected in the SPIRE spectrum, and may also arise in the background.

(vii) Our results indicate that η Car's small reservoir of carbon is held in C-bearing molecules. CO in particular mainly traces the inner layers of the expanding Butterfly Nebula associated with the massive disrupted torus (see Fig. 1). No C-bearing dust species have been identified in η Car's complex solid state spectrum, while the *N*-rich atomic and molecular gas appears to provide favourable conditions for the formation of AlN and Si_3N_4 dust in low abundances (Morris et al. 2017).

(viii) Emission lines from most of the molecules listed in Table 3 are detected in the central spaxel of PACS (HCl is detected in the SPIRE spectrum), but outside of CO and NH, they are generally too weak or blended to determine their extent in the rest of the nebula. We know from ground-based and HIFI observations, however, that *N*-bearing molecules NH_2, N_2H^+, CN, HCN, and HNC all share a very similar velocity structure with CO, and are thus principally associated with inner layers of the dusty equatorial torus. Certain molecules such as CH_3OH and possibly NH_3 and H_2O are more centrally confined, $\lesssim$2 arcsec across, possibly tracing shock-heated gas.

4.2.1 *Abundance patterns*

The abundance pattern resulting from our broad-brush modeling of η Car's submillimetre line spectrum provides further support for the Homunculus and its interior structures having been formed in explosive events from at least one massive star (but possible two in a merger scenario) with surface abundances consistent with yields and elemental depletions resulting from CNO cycle. While precise abundance estimates are hindered by certain necessary simplifying assumptions on the geometry of the line emitting regions and interactions with the thermal continuum, the scales of the abundances certainly point to an *N*-rich, *C*-deficient environment with temperatures and densities supporting the formation and survival of molecules with upper level energies up to ∼500 K, and no more complex than CH_3OH (so far).

The derived[CO/H_2] and [$^{12}C/^{13}C$] abundance ratios of 2.0×10^{-5} and ∼3–4, respectively, are both quite low compared to cosmic abundances (by factors of 10-20 each), as expected from evolutionary models for the depletion of ^{12}C and enhancement of ^{13}C for rotating massive starts prior to entering the core He-burning phase of Wolf–Rayet stars (e.g. Ekström et al. 2012). Our results are consistent with those of Morris et al. (2017, 2020) who analysed velocity-resolved HIFI and *ALMA* CO observations.

The numerous transitions from *N*-bearing molecules in the *ISO* scans are evidence of the nitrogen-rich environment; however, our results for the abundances of the *N* hydrides may be several factors to an order of magnitude in error, in part because they are distributed on different spatial scales, although the Butterfly Nebula always dominates the emission. NH is found throughout the Homunculus (Section 3.1.9), including fast-moving material possibly located in the thin walls of the two lobes and/or the skirt. The velocity structure of NH_2 and N_2H^+ from HIFI and *ALMA* observations show a closer association with the expanding Butterfly Nebula, while NH_3 may be more closely confined to the compact central source (Smith 2006). The main effect will be on the estimated column densities, decreasing $\mathcal{N}$(NH) and increasing $\mathcal{N}(NH_3)$ such that the $NH/NH_2/NH_3$ abundance ratio should be qualitatively taken as (<2.0)/1.0/(>0.4).

Not surprisingly, the $NH/NH_2/NH_3$ ratio trends opposite of that estimated from absorption lines towards Sgr B2 star-forming clouds Goicoechea, Rodríguez-Fernández & Cernicharo (2004) and in cold envelopes around protostellar cores (e.g. Hily-Blant et al. 2010) where collisional processes are weak at low temperatures, and NH is observed in smallest relative abundance, NH_3 the highest, separated by two orders or magnitude. Surprisingly, the $NH/NH_2/NH_3$ ratio is *very* similar to those deduced from absorption lines in the diffuse or translucent sightlines studied by Persson et al. (2012), indeed almost *equivalent* towards the massive star-forming region G10.6−0.4. This is probably coincidental. The densities, column densities, and radiation environments are very different in eta Car compared with diffuse molecular gas in the Galactic plane.

4.2.2 *Theoretical considerations*

Potentially, more important to the veracity of the abundances than simplifying the geometry of the line forming gas (which we can eventually account for more accurately with, e.g. *ALMA* observations) is a full accounting of the physical processes which drive excitation, including collisional excitation, radiative excitation, spontaneous radiative decay, and formation pumping. LTE will be reached through collisions at sufficiently high gas densities, populating energy levels at the gas kinetic temperature. However, as summarized by Gerin, Neufeld & Goicoechea (2016; see also Roueff & Lique 2013), the smaller momenta of inertia, larger rotational constants, and much higher spontaneous radiative decay rates for the rotational states of the hydrides compared to other molecules result in much higher densities needed to achieve LTE. Below such 'critical' densities, excitation becomes subthermal as total production and loss rates reach a state of quasi-equilibrium, and the excitation temperatures for most transitions are lower than the gas kinetic temperature. We demonstrated in our analysis of the mid-IR and submillimetre H I lines that departures from LTE occur due to radiative coupling of the Rydberg states to the strong thermal continuum.

The molecular abundances and ionization may be partly controlled by radiative processes in the Homunculus, in the presence of the X-ray and UV radiation field of the hot, luminous stellar pair at the centre. Energetic photons attenuated by complex shielding conditions in the Homunculus will dissociate and ionize molecules and atoms with ionization potentials below 13.6 eV, to an extent determined by the hardness of the photodissociation region (PDR). η Car is a source of X-ray emission (Pittard & Corcoran 2002), and a diagnostic of the hardness of the radiation field incident on the gas may be found in the HNC/HCN line ratio. It has been suggested that molecular line intensity ratios, e.g. HNC/HCN, can distinguish between X-ray-dominated (XDR) and UV-photon-dominated (PDR) regions in luminous infrared galaxies (Meijerink, Spaans & Israel 2007). Such claims are model dependent. Further investigation of the photochemistry and ionization in eta Car might lead to a better understanding of other such complex, dust-obscured environments.

Shielding is provided mainly by the enormous torus-like structure where the bulk of the 0.22 $M_\odot$ of dust resides, but also in material in the poorly understood immediate vicinity of the binary, containing an unknown fraction of vibrationally excited H_2 (which is a key component in energetic reactions; e.g. Black & van Dishoeck 1987;

Agúndez et al. 2010), and dense 'coronagraphic' structures of unknown distance from the central source Damineli et al. (2019), possibly associated with the compact source of methanol, water, and ammonia (Smith 2006; Morris et al. 2020). These species are sometimes considered as tracers of shock-heated gas, which has not been treated in our modelling.

Shocks are expected to have a significant effect on the chemistry of the nebula, with the destruction of certain molecules and enhancement of others. Many of the species we have observed but especially NH_3, CH_3OH, H_2O, and CH^+ may be useful as indicators of shock-heated gas in different parts of the Homunculus and central region. While we cannot easily follow up with H_2O observations from the ground or with SOFIA instruments (except in very excited states), further observations of OH should be rewarding if at the high temperatures of the gas, most of the gas-phase oxygen is driven into OH in collisions with vibrationally excited, or simply hot, molecular hydrogen H_2^*, and then into water $OH + H_2^* \rightarrow H_2O + H$. The balance of OH and H_2O in both forward and reverse reactions in the nebula will be regulated by the local UV field strength or shock velocities. This is a topic we will address in a future study of the chemistry-driving roles of UV irradiation and shocks in η Car, requiring additional high-angular observations to disentangle the kinematics of the bulk motion of structures in and around the central region from shock-broadened emission.

4.3 The uniqueness of η Car

Most evolved stars with mass-loss have circumstellar envelopes that are rich in carbon or oxygen at the expense of nitrogen through the CNO cycle. AGB stars (initial masses, $M \approx$ 1–8$M_\odot$) and RSG stars ($M \approx$ 8–30 $M_\odot$) have circumstellar shells rich in oxygen- and carbon-bearing molecules. In contrast, the ejecta around η Car contain proportionately more nitrogen-bearing molecules compared to circumstellar envelopes around less-massive, evolved stars. Such would be expected given the strong nitrogen presence and near-absence of oxygen and carbon in the ionized ejecta as noted previously by Davidson et al. (1986) and Verner et al. (2005b), as there is little evidence of abundance stratification in the ejecta. The overabundance of nitrogen plus the detected C/O < 4 is consistent with the ejecting star having an initial mass > 60 $M_\odot$ (Ekström et al. 2012).

The massive binary, η Car, has gone through a transition on historical timescales and is sufficiently close that present observatories can study the ejecta in detail. This system is providing ample information on binary systems with stellar members greatly exceeding 30 $M_\odot$. At any given epoch, the more massive stars, like those found in η Car, occur far less frequently, their lifetimes are also much shorter, and likely contribute significantly to enrichment of the interstellar medium. What is learned from this massive binary has potential impact on our knowledge of the earliest stars in our Universe, the massive members of which evolved on rapid timescales quickly enriching the ISM and may be revealing information on Type IIn or Ib/c progenitors.

ACKNOWLEDGEMENTS

The content of this paper is based on observations with the *Herschel Space Observatory*, which is an ESA space observatory with science instruments provided by European-led Principal Investigator consortia and with important participation from NASA. We have made use software in the *Herschel* Interactive Processing Environment (HIPE), which was a joint development by the *Herschel* Science Ground Segment Consortium, consisting of ESA, the NASA Herschel Science Center, and the HIFI, PACS and SPIRE consortia. TRG, KEN, and PM acknowledge partial financial support from NASA grant SCEX22012D for the *Herschel* programme OT1_tgull3. MJB acknowledges support from European Research Council Grant SNDUST ERC-2015-AdG-694520. TRG acknowledges the support of Onsala Observatory and Max Planck Institute for RadioAstronomy during visits at those institutions.

We thank the referee for many useful comments leading to significant improvement of this paper.

DATA AVAILABILITY

The observations presented in this paper are based on observations which are available in the public *Herschel* http://archives.esac.esa.int/hsa/whsa/ and *ISO* data archives https://www.cosmos.esa.int/web/iso/. Reasonable requests for advanced data products may be addressed to P.W.M.

REFERENCES

Abraham Z., Falceta-Gonçalves D., Beaklini P. P. B., 2014, ApJ, 791, 95
Agúndez M., Goicoechea J. R., Cernicharo J., Faure A., Roueff E., 2010, ApJ, 713, 662
Artigau É., Martin J. C., Humphreys R. M., Davidson K., Chesneau O., Smith N., 2011, AJ, 141, 202
Black J. H., van Dishoeck E. F., 1987, ApJ, 322, 412
Bocchio M., Bianchi S., Abergel A., 2016, A&A, 591, A117
Brown, J. M., Schubert, J. E ., Evenson K. M., Radford, H. E, 1982, ApJ, 258, 899
Brown, J. M., Varberg,T.D. , Evenson, K. M., Cooksy, A., 1994, ApJL, 428, L37
Chesneau O. et al., 2005, A&A, 435, 1043
Cox P., Mezger P. G., Sievers A., Najarro F., Bronfman L., Kreysa E., Haslam G., 1995, A&A, 297, 168
Currie D. G., Dorland B. N., Kaufer A., 2002, A&A, 389, L65
Damineli A., 1996, ApJ, 460, L49
Damineli A. et al., 2019, MNRAS, 484, 1325
Davidson K., 1997, New Astron., 2, 387
Davidson K., Dufour R. J., Walborn N. R., Gull T. R., 1986, ApJ, 305, 867
Davidson K., Walborn N. R., Gull T. R., 1982, ApJ, 254, L47
de Graauw T. et al., 1996, A&A, 315, L49
Dorland B. N., 2007, PhD thesis, Univ. Maryland, College Park
Duncan R. A., White S. M., 2003, MNRAS, 338, 425
Ekström S. et al., 2012, A&A, 537, A146
Flower,D. R. , Seaton, M. J. 1969, CoPhC 1, 31F
Frew D. J., 2004, J. Astron. Data, 10, 6
Gerin M., Neufeld D. A., Goicoechea J. R., 2016, ARA&A, 54, 181
Goicoechea J. R., Rodríguez-Fernández N. J., Cernicharo J., 2004, ApJ, 600, 214
Grant D., Blundell K., Matthews J., 2020, MNRAS, 494, 17
Griffin M. J. et al., 2010, A&A, 518, L3
Groh J., Meynet G., Ekstrom S., Georgy C., 2014, A&A, 564, A30
Groh J. H., Hillier D. J., Madura T. I., Weigelt G., 2012, MNRAS, 423, 3024
Gull T. R., Kober G. V., Nielsen K. E., 2006, ApJS, 163, 173
Gull T. R. et al., 2009, MNRAS, 396, 1308
Gull T. R. et al., 2016, MNRAS, 462, 3196
Hartman H., Gull T., Johansson S., Smith N., *HST Eta Carinae Treasury Project Team*, 2004, A&A, 419, 215
Hillier D. J., Davidson K., Ishibashi K., Gull T., 2001, ApJ, 553, 837
Hily-Blant P. et al., 2010, A&A, 521, L52
Hopwood R. et al., 2015, MNRAS, 449, 2274
Hummer D. G., Storey P. J., 1987, MNRAS, 224, 801
Indebetouw R. et al., 2005, ApJ, 619, 931
Ishibashi K. et al., 2003, AJ, 125, 3222
Kessler M. F. et al., 1996, A&A, 500, 493
Kiminki M. M., Reiter M., Smith N., 2016, MNRAS, 463, 845

Loinard L., Kamiński T., Serra P., Menten K. M., Zapata L. A., Rodríguez L. F., 2016, ApJ, 833, 48
Loinard L., Menten K. M., Güsten R., Zapata L. A., Rodríguez L. F., 2012, ApJ, 749, L4
Madura T. I. et al., 2013, MNRAS, 436, 3820
Mauerhan J. C. et al., 2013, MNRAS, 430, 1801
Mehner A., Davidson K., Ferland G. J., Humphreys R. M., 2010, ApJ, 710, 729
Mehner A. et al., 2016, A&A, 595, A120
Mehner A. et al., 2019, A&A, 630, L6
Meijerink R., Spaans M., Israel F. P., 2007, A&A, 461, 793
Mookerjea B., Sandell G., Güsten R., Riquelme D., Wiesemeyer H., Chambers E., 2019, A&A, 626, A131
Morris P. W., Gull T. R., Hillier D. J., Barlow M. J., Royer P., Nielsen K., Black J., Swinyard B., 2017, ApJ, 842, 79
Morris P. W. et al., 1999, Nature, 402, 502
Morris P. W. et al., 2020, ApJ, 892, L23
Müller H. S. P., Schlöder F., Stutzki J., Winnewisser G., 2005, J. Mol. Struct., 742, 215
Nielsen K. E., Gull T. R., Vieira Kober G., 2005, ApJS, 157, 138
Oberst T. E., Parshley S. C., Nikola T., Stacey G. J., Löhr A., Lane A. P., Stark A. A., Kamenetzky J., 2011, ApJ, 739, 100
Persson C. M. et al., 2012, A&A, 543, A145
Pickett H. M., Poynter R. L., Cohen E. A., Delitsky M. L., Pearson J. C., Müller H. S. P., 1998, J. Quant. Spec. Radiat. Transf., 60, 883
Pilbratt G. L. et al., 2010, A&A, 518, L1
Pittard J. M., Corcoran M. F., 2002, A&A, 383, 636
Poglitsch A. et al., 2010, A&A, 518, L2
Polomski E. F., Telesco C. M., Piña R. K., Fisher R. S., 1999, AJ, 118, 2369
Roelfsema P. R. et al., 2012, A&A, 537, A17
Roueff E., Lique F., 2013, Chem. Rev., 113, 8906
Smith N., 2002, MNRAS, 337, 1252
Smith N., 2006, ApJ, 644, 1151
Smith N., 2008a, in de Koter A., Smith L. J., Waters L. B. F. M., eds, ASP Conf. Ser. Vol. 388, Mass Loss from Stars and the Evolution of Stellar Clusters. Astron. Soc. Pac., San Francisco, p. 129
Smith N., 2008b, Nature, 455, 201
Smith N., Brooks K. J., Koribalski B. S., Bally J., 2006, ApJ, 645, L41
Smith N., Gehrz R. D., 1998, AJ, 116, 823
Smith N., Gehrz R. D., Hinz P. M., Hoffmann W. F., Hora J. L., Mamajek E. E., Meyer M. R., 2003, AJ, 125, 1458
Smith N., Ginsburg A., Bally J., 2018a, MNRAS, 474, 4988
Smith N., Morse J. A., 2004, ApJ, 605, 854
Smith N. et al., 2018b, MNRAS, 480, 1466
Steffen W. et al., 2014, MNRAS, 442, 3316
Swinyard B. M. et al., 2010, A&A, 518, L4
Swinyard B. M. et al., 2014, MNRAS, 440, 3658
Teodoro M., Gull T. R., Bautista M. A., Hillier D. J., Weigelt G., Corcoran M. F., 2020, MNRAS, 495, 2754
Teodoro M., Madura T. I., Gull T. R., Corcoran M. F., Hamaguchi K., 2013, ApJ, 773, L16
Teodoro M. et al., 2016, ApJ, 819, 131
Valentijn E. A. et al., 1996, A&A, 315, L60
Valtchanov I. et al., 2018, MNRAS, 475, 321
van der Tak F. F. S., Black J. H., Schöier F. L., Jansen D. J., van Dishoeck E. F., 2007, A&A, 468, 627
Verner E., Bruhweiler F., Nielsen K. E., Gull T. R., Vieira Kober G., Corcoran M., 2005b, ApJ, 629, 1034
Verner E. M., Bruhweiler F., Gull T. R., 2005a, ApJ, 624, 973
Walborn N. R., Blanco B. M., Thackeray A. D., 1978, ApJ, 219, 498
Weigelt G, Kraus S., 2012, in Davidson K., Humphreys R. M., eds, Astrophysics and Space Science Library Vol. 384, Eta Carinae and the Supernova Impostors, Springer, New York. p. 129
Weigelt G., Ebersberger J., 1986, A&A, 163, L5
Weis K., Duschl W. J., Bomans D. J., Chu Y.-H., Joner M. D., 1997, A&A, 320, 568
Weis K., Duschl W. J., Chu Y.-H., 1999, A&A, 349, 467
Westphal J. A., Neugebauer G., 1969, ApJ, 156, L45
Wu R. et al., 2013, A&A, 556, A116
Zethson T., Gull T. R., Hartman H., Johansson S., Davidson K., Ishibashi K., 2001, AJ, 122, 322
Zethson T., Johansson S., Hartman H., Gull T. R., 2012, A&A, 540, A133

APPENDIX A: SPIRE SPECTRUM AND LINE IDENTIFICATION

The complete SPIRE spectrum is plotted in Figs A1–A13 extending from 14.9 to 52.4 cm^{-1}. Note that the spectrum is less reliable beyond 51.5 cm^{-1} with the last line identification being at 51.4 cm^{-1}.

Table A1 lists line identifications and measures for the more prominent, relatively isolated emission features. While the S/N exceeds 100, the spectral resolution of SPIRE and spatial resolution of *Herschel Space Observatory* limit line identifications. As noted in the introduction (Section 1) and demonstrated in the PACS Data Analysis (SubSection 3.1), known structures of the ejecta extend from the subarcsecond Weigelt clumps near η Car to the 4 arcsec diameter cavity of the Butterfly Nebula, the 10 arcsec × 20 arcsec Homunculus to external fast moving knots at distances of 30 arcsec from η Car (Smith 2008b; Kiminki et al. 2016). The foreground lobe of the Homunculus is expanding at −600 km s^{-1} and the background lobe at +600 km s^{-1}. Radio observations of the H I recombination lines (Duncan & White 2003) constrain the ionized hydrogen region to 0.5 arcsec while the PACS studies of [C II] (subSection 3.1.8) and NH (subSection 3.1.9) demonstrate these emissions originate from the Homunculus.

Improved line identifications must wait for future observations of higher angular and spectroscopic resolutions that will reveal resolved structures and thus provide greatly improved models of the complex ejecta.

The spectral nomenclature in Table A1 and Fig. A1 for atomic transitions refers to the principal quantum numbers, n, of the transitions (Example: H I (21 − 20)).For molecular transitions a variety of notations is needed. When there is unresolved fine- and hyperfine structure, only the leading rotational or angular-momentum quantum numbers are listed (Example: NH_2 3(12) − 3(03).

Where blends are obvious, the measurement is placed with the line identification closest to the measured line and the apparently weaker line is noted to be blended. (Example at 30.350 cm^{-1} in Fig. A6 three lines appear to be blended. The wavelength closest to that measured is 30.244 cm^{-1} identified as CN (8 − 7). The line identifications HCN (10 − 9) and NH_2 2(02)−1(11) are listed as blended in the comments column. Fluxes are listed along with measurement error for most lines. Lines considered to be present, but too weak for accurate measure are noted as weak in the comment column.

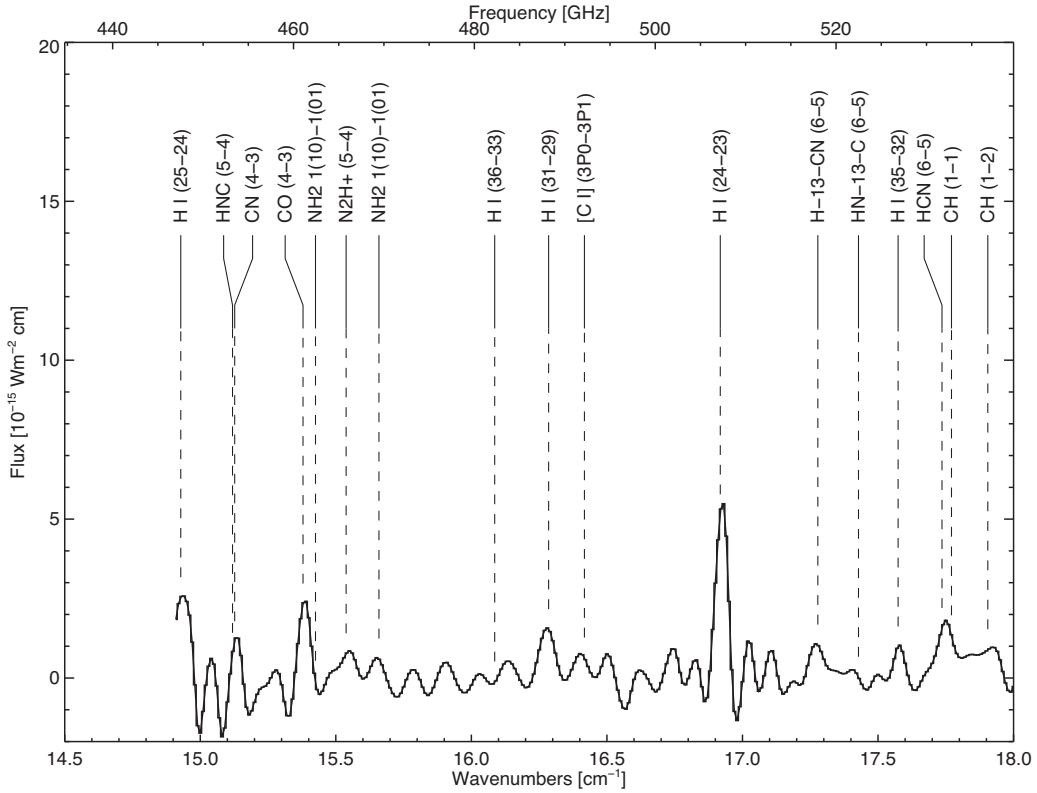

Figure A1. SPIRE spectrum 14.5–18.0 cm^{-1}. As commented in Section 2.2, the S/N exceeds 100 over most of the spectrum depicted in Figs A1 through A13. Most of the features in these spectra are real and promise to reveal even more line identifications. Note that, for all of the following spectral plots, the strong continuum has been subtracted to provide an optimized baseline for line identification.

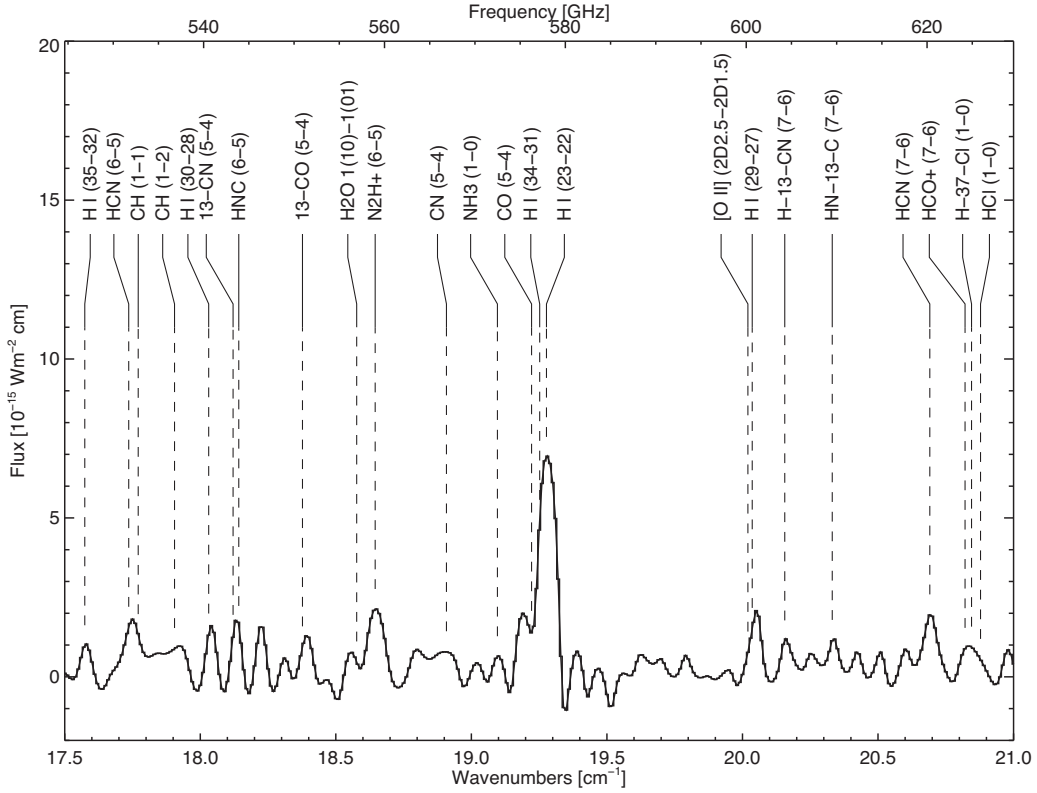

Figure A2. SPIRE spectrum 17.5–21.0 cm^{-1}.

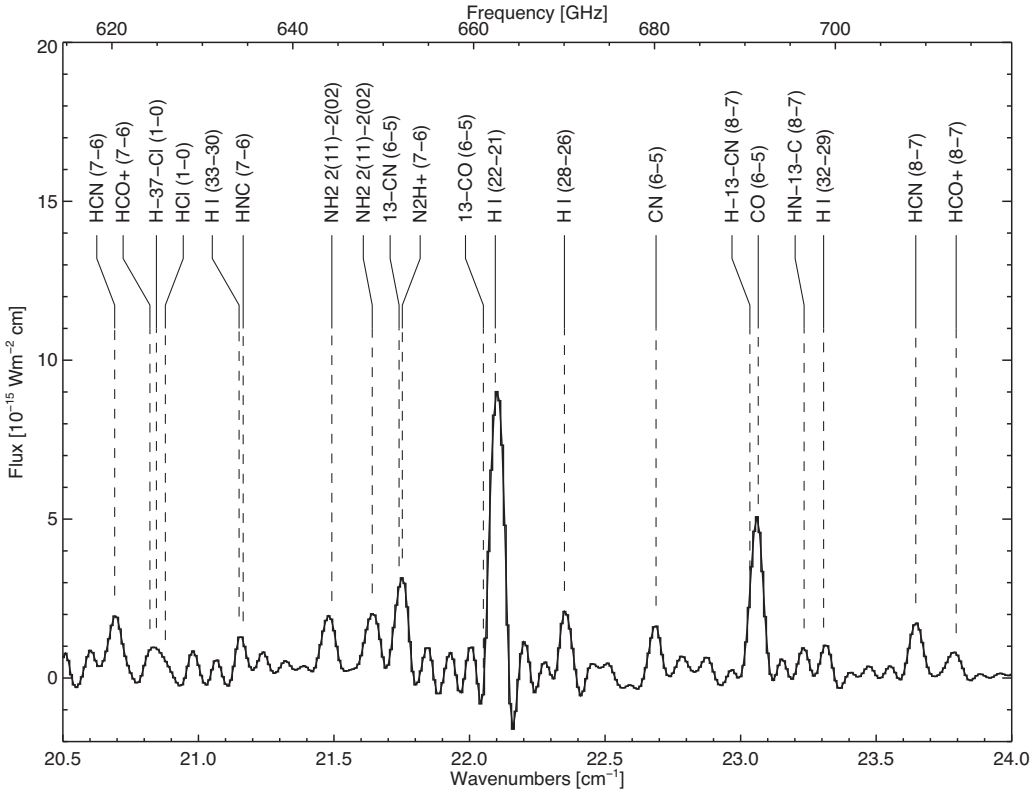

Figure A3. SPIRE spectrum 20.5–24.0 cm^{-1}.

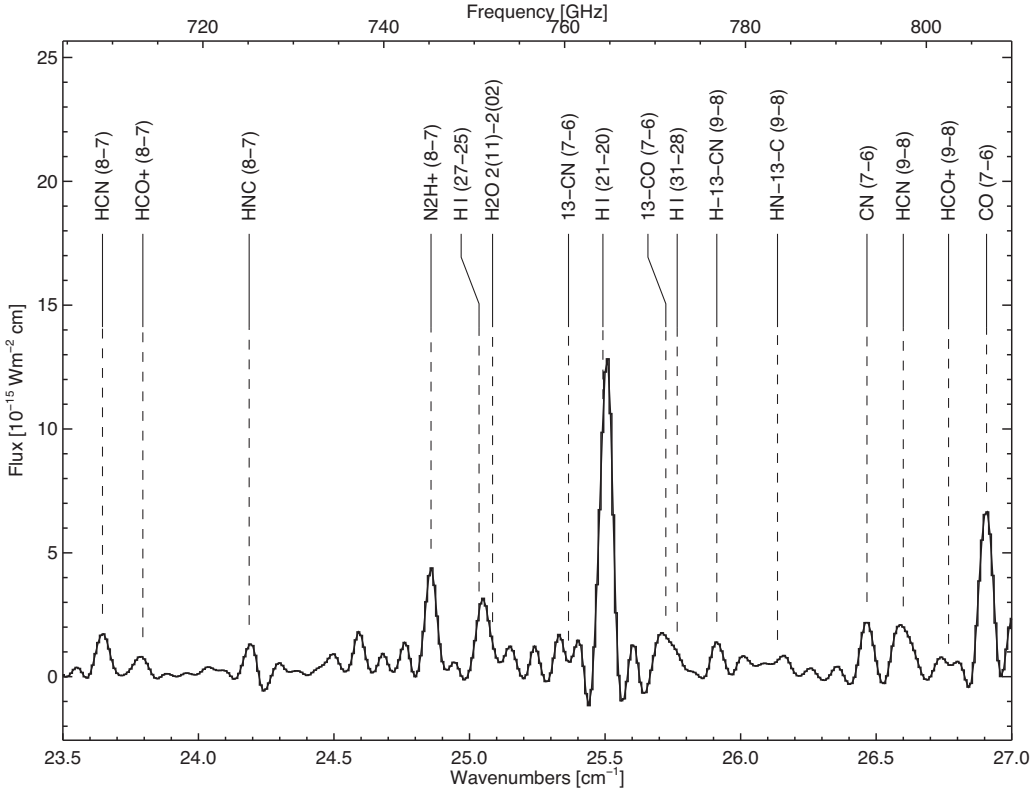

Figure A4. SPIRE spectrum 23.5–27.0 cm^{-1}.

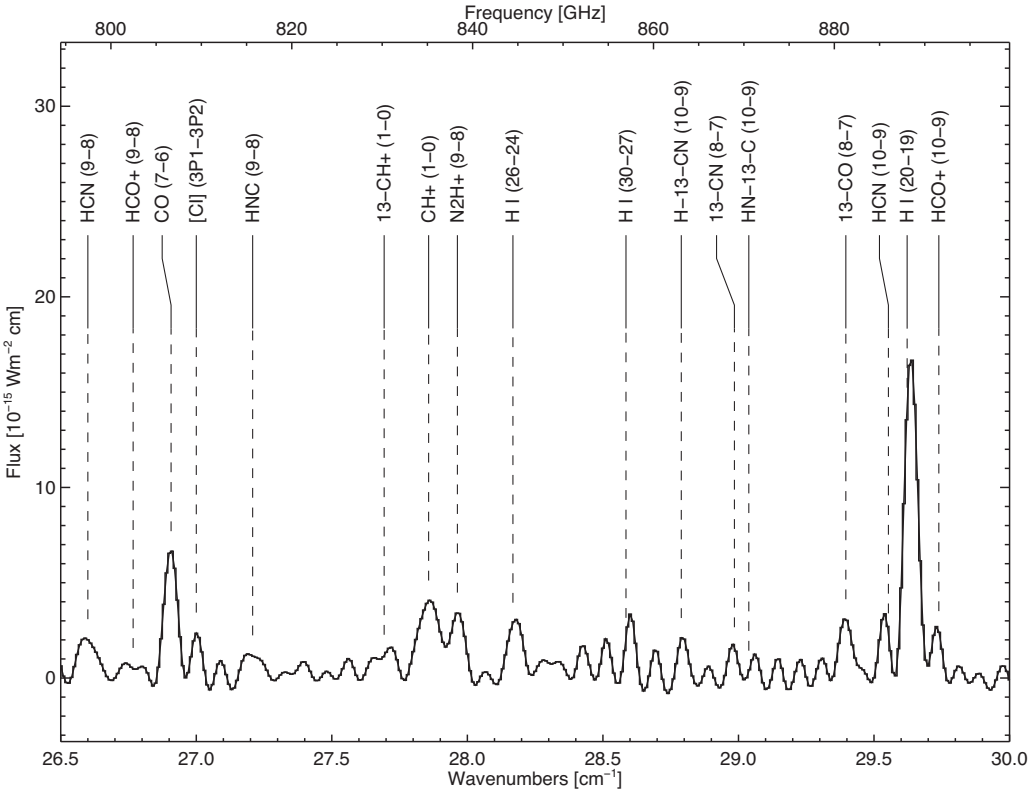

Figure A5. SPIRE spectrum 26.5–30.0 cm^{-1}.

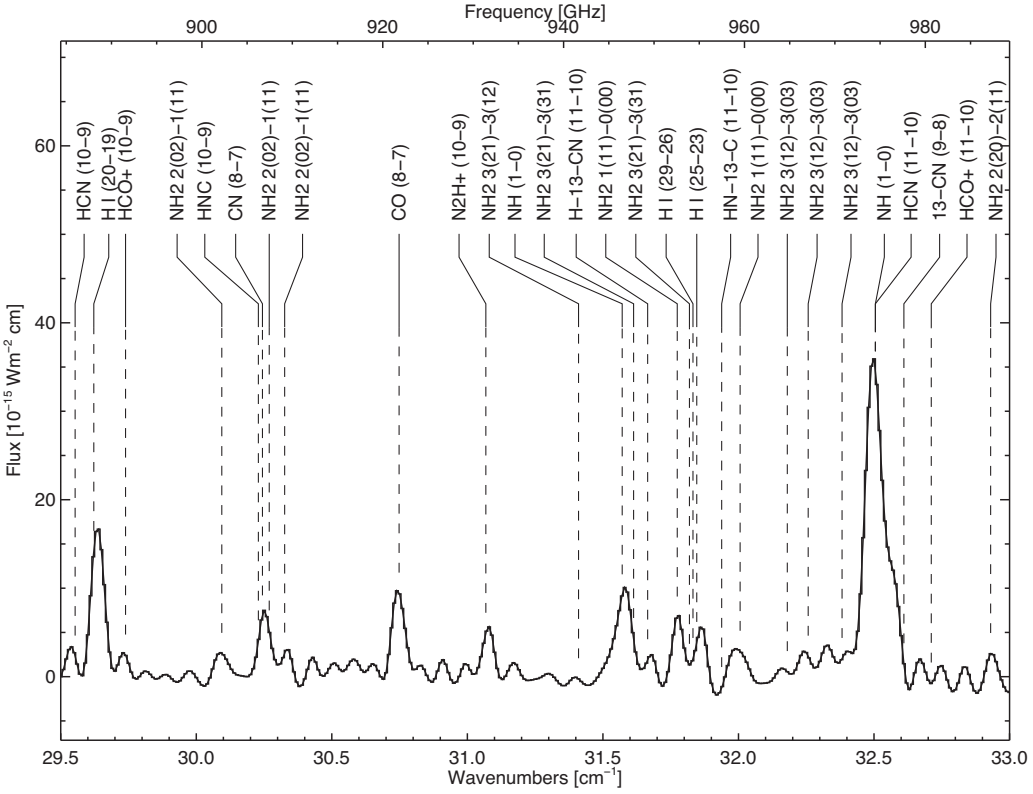

Figure A6. SPIRE spectrum 29.5–33.0 cm^{-1}.

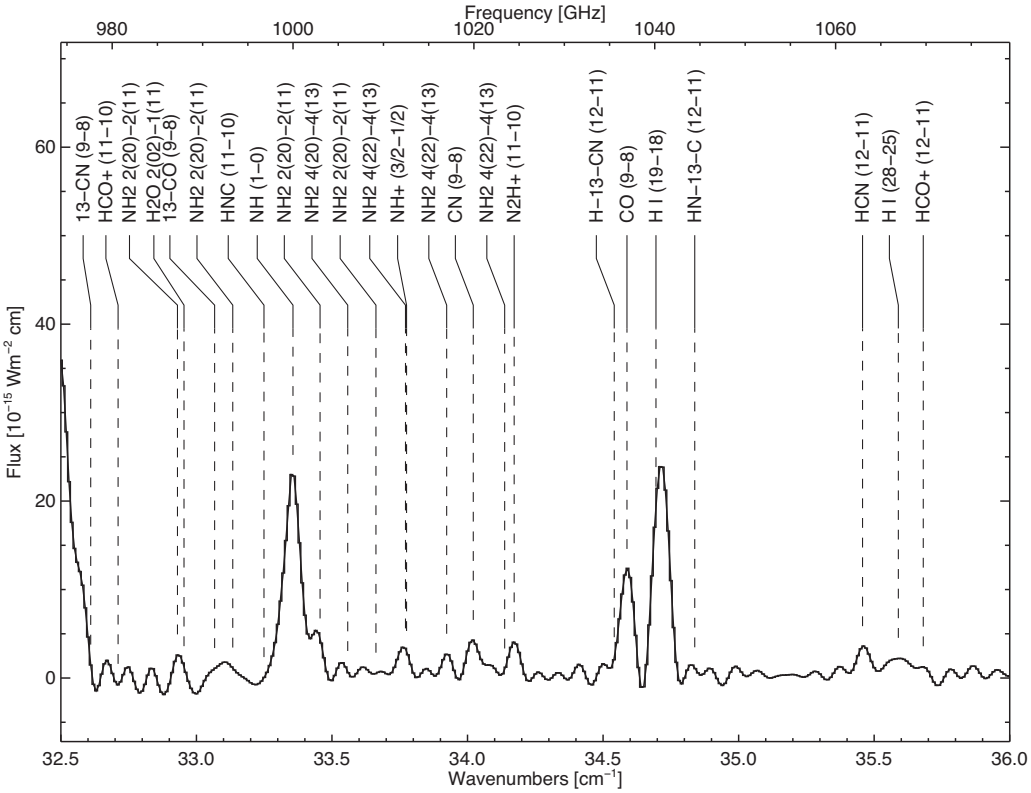

Figure A7. SPIRE spectrum 32.5–36.0 cm^{-1}.

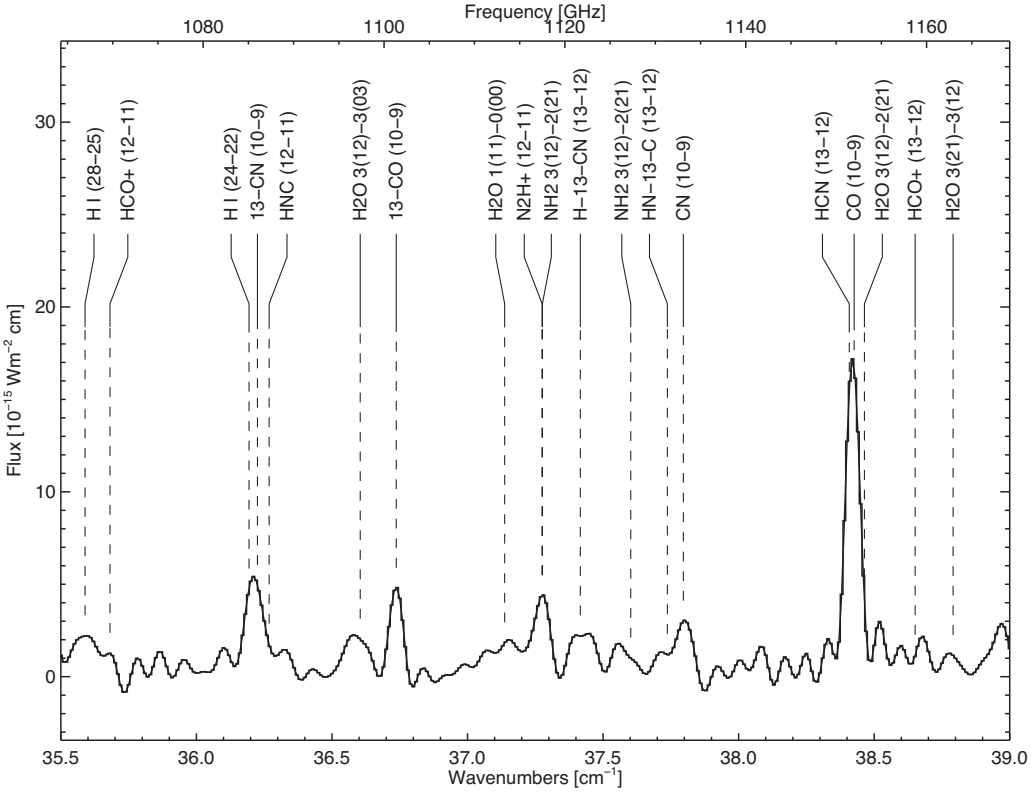

Figure A8. SPIRE spectrum 35.5–39.0 cm^{-1}.

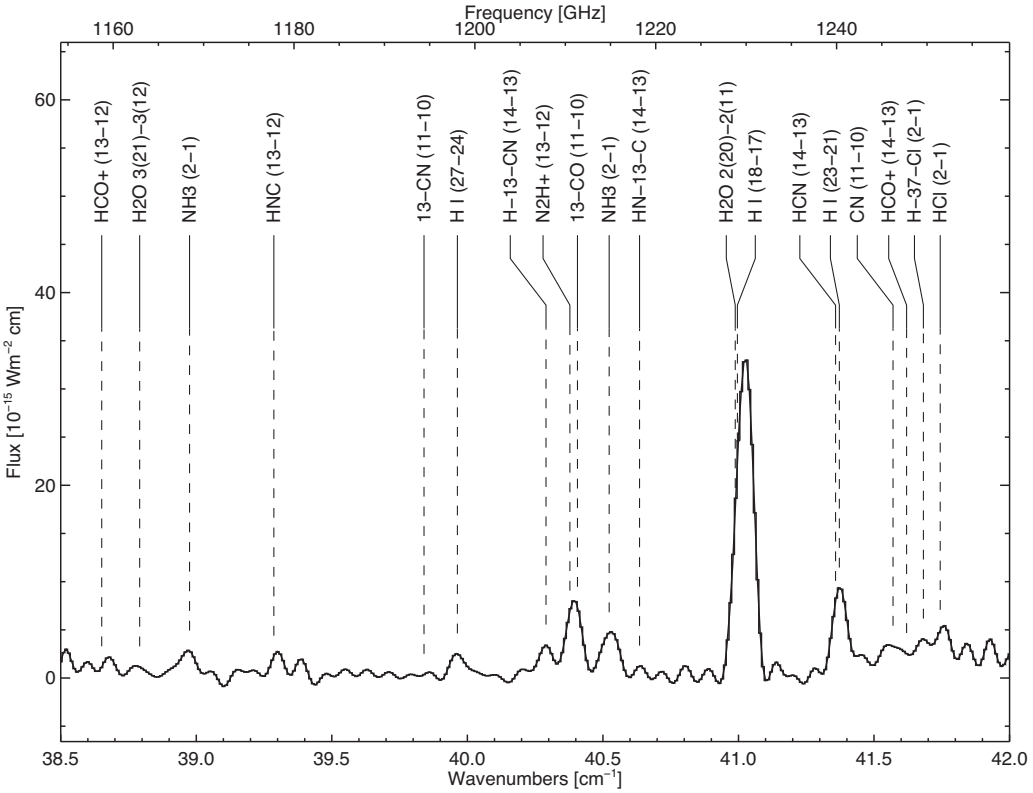

Figure A9. SPIRE spectrum 38.5–42.0 cm^{-1}.

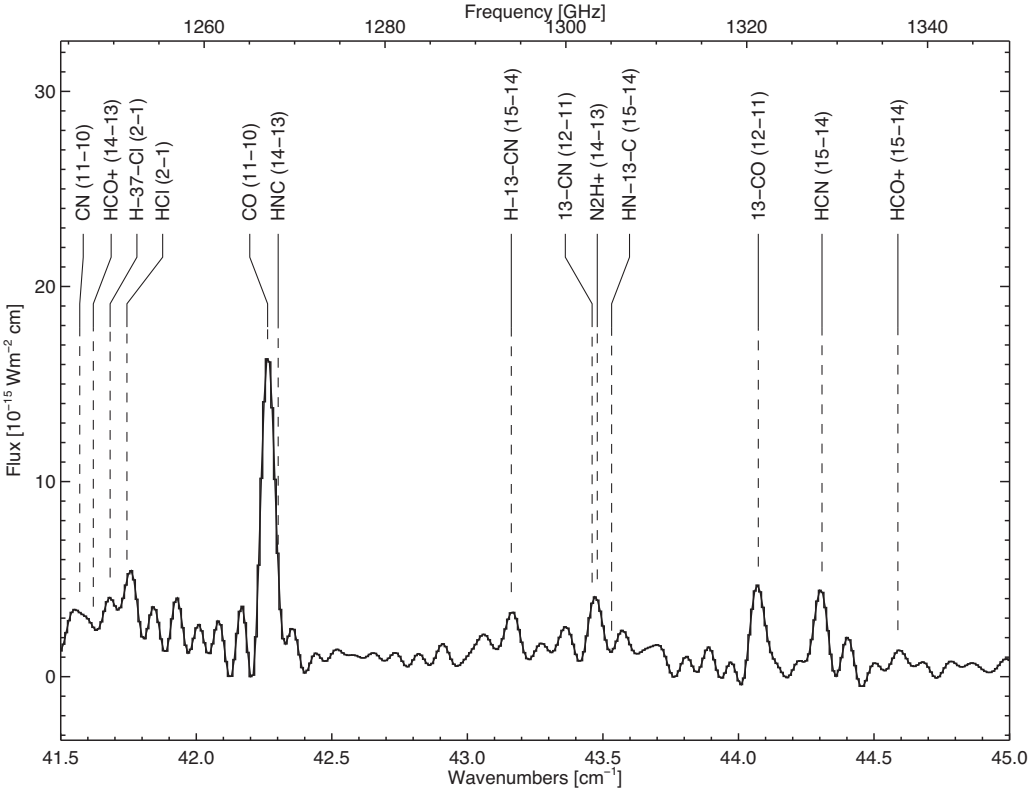

Figure A10. SPIRE spectrum 41.5–45.0 cm^{-1}.

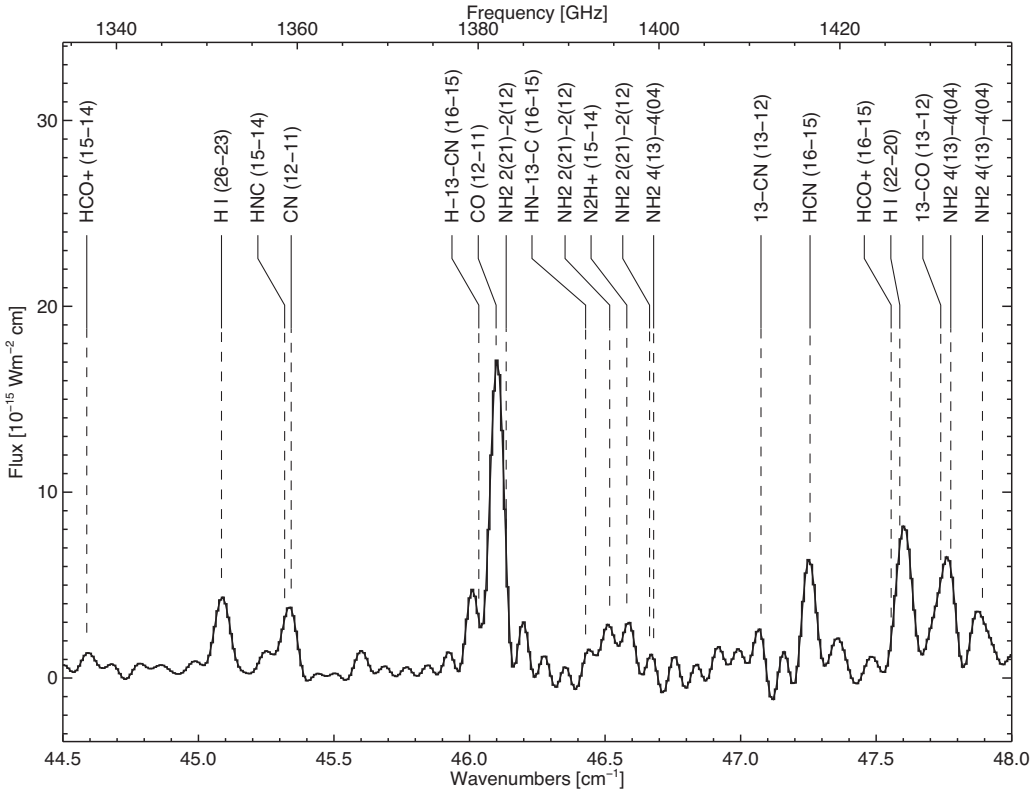

Figure A11. SPIRE spectrum 44.5–48.0 cm^{-1}.

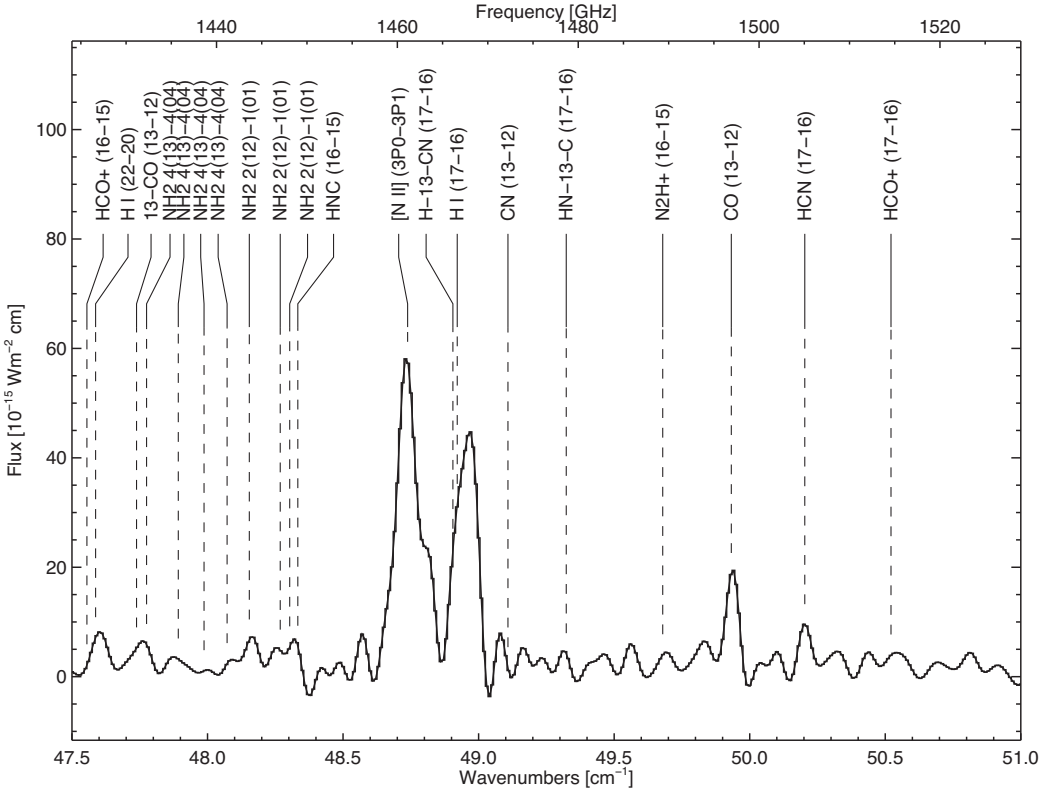

Figure A12. SPIRE spectrum 47.5–51.0 cm^{-1}.

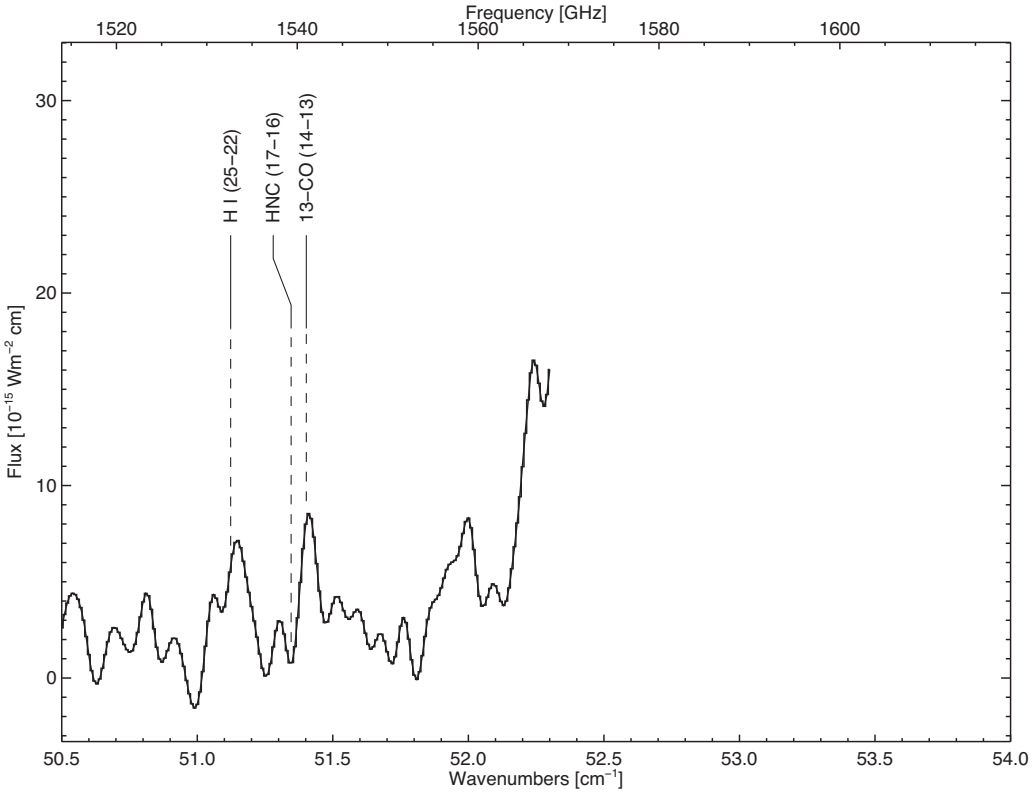

Figure A13. SPIRE spectrum 50.5–54.0 cm^{-1} Note that while the plot extends out to 52.3 cm^{-1}, the spectrum is not reliable beyond 51.5 cm^{-1} with the last line tabulated in Table A1 at 51.4 cm^{-1}.

Table A1. Line Identifications from the SPIRE spectrum.

Wavenumber (cm^{-1})	Frequency (GHz)	Identification (cm^{-1})	Measured (10^{-17}Wm^{-2})	Line Flux	Comments
14.928	447.53	H I (25 − 24)	14.926	24.70 (0.70)	
15.127	453.50	CN (4 − 3)	15.131	5.43 (0.61)	bl. HNC (5 − 4)
15.379	461.05	CO (4 − 3)	15.373	9.31 (0.88)	
15.538	465.82	N_2H^+ (5 − 4)	15.539	6.86 (0.61)	bl. NH_2 1(10)−1(01)
15.659	469.45	NH_2 1(10)−1(01)			Weak
16.086	482.25	H I (36 − 33)	16.089	4.49 (0.61)	
16.285	488.21	H I (31 − 29)	16.289	6.20 (0.61)	
16.417	492.17	[C I] ($^3P_0$−$^3P_1$)			Weak
16.918	507.19	H I (24 − 23)	16.922	27.75 (0.65)	
17.278	517.98	H^{13}CN (6 − 5)	17.269	3.74 (0.60)	
17.428	522.48	HN^{13}C (6 − 5)	17.428	4.52 (0.61)	
17.574	526.86	H I (35 − 32)	17.583	5.24 (0.55)	
17.736	531.71	HCN (6 − 5)	17.747	12.47 (0.56)	bl. CH (1 − 1)
17.905	536.78	CH (1 − 2)	17.896	7.92 (0.56)	
18.031	540.56	H I (30 − 28)	18.032	7.41 (0.55)	
18.142	543.88	HNC (6 − 5)	18.140	4.75 (0.55)	bl.^{13}CN (5 − 4)
18.377	550.93	^{13}CO (5 − 4)	18.381	5.17 (0.55)	
18.577	556.92	H_2O 1(10)−1(01)	18.558	1.77 (0.58)	
18.645	558.96	N_2H^+ (6 − 5)	18.634	12.50 (0.58)	
18.908	566.85	CN (5 − 4)	18.917	7.42 (0.55)	
19.096	572.48	NH_3 (1 − 0)			Weak
19.222	576.26	CO (5 − 4)	19.207	9.25 (0.74)	
19.277	577.91	H I (23 − 22)	19.276	45.31 (0.87)	bl. H I (34 − 31)
20.036	600.66	H I (29 − 27)	20.038	8.31 (0.55)	bl. [O II] ($^2D_{2.5}$−$^2D_{1.5}$)
20.156	604.26	H^{13}CN (7 − 6)	20.147	3.83 (0.54)	
20.331	609.51	HN^{13}C (7 − 6)	20.344	2.36 (0.60)	
20.691	620.30	HCN (7 − 6)	20.689	9.45 (0.55)	
20.821	624.20	HCO^+ (7 − 6)	20.824	4.20 (0.89)	

Table A1 – *continued*

Wavenumber (cm^{-1})	Frequency (GHz)	Identification (cm^{-1})	Measured ($10^{-17}Wm^{-2}$)	Line Flux	Comments
20.878	625.91	HCl (1 − 0)	20.869	1.01 (0.78)	bl. $H^{37}Cl$ (1 − 0)
21.165	634.51	HNC (7 − 6)	21.155	7.76 (0.57)	bl. H I (33 − 30)
21.492	644.31	NH_2 2(11)−2(02)	21.487	11.07 (0.57)	
21.641	648.78	NH_2 2(11)−2(02)	21.642	12.23 (0.57)	
21.752	652.11	N_2H^+ (7 − 6)	21.748	19.60 (0.58)	bl.^{13}CN (6 − 5)
22.095	662.39	H I (22 − 21)	22.100	53.00 (0.64)	bl. ^{13}CO (6 − 5)
22.350	670.04	H I (28 − 26)	22.353	9.55 (0.57)	
22.688	680.17	CN (6 − 5)	22.686	9.21 (0.57)	
23.065	691.47	CO (6 − 5)	23.059	28.85 (0.59)	bl. $H^{13}CN$ (8 − 7)
23.234	696.54	$HN^{13}C$ (8 − 7)			Weak
23.306	698.70	H I (32 − 29)	23.306	6.18 (0.57)	
23.646	708.89	HCN (8 − 7)	23.644	11.95 (0.58)	
23.795	713.36	HCO^+ (8 − 7)			Weak
24.187	725.11	HNC (8 − 7)	24.187	5.59 (0.70)	
24.858	745.22	N_2H^+ (8 − 7)	24.854	17.34 (0.71)	
25.035	750.53	H I (27 − 25)	25.050	15.06 (0.71)	bl. H_2O 2(11)−2(02)
25.365	760.42	^{13}CN (7 − 6)			Weak
25.492	764.23	H I (21 − 20)	25.502	64.69 (0.82)	
25.724	771.19	^{13}CO (7 − 6)	25.719	6.73 (1.43)	
25.766	772.45	H I (31 − 28)	25.760	3.80 (0.14)	
25.912	776.82	$H^{13}CN$ (9 − 8)	25.911	6.71 (0.71)	
26.136	783.54	$HN^{13}C$ (9 − 8)	26.142	4.59 (0.75)	
26.466	793.43	CN (7 − 6)	26.462	11.06 (0.70)	
26.600	797.45	HCN (9 − 8)	26.582	9.23 (1.68)	
26.767	802.45	HCO^+ (9 − 8)			Weak
26.907	806.65	CO (7 − 6)	26.905	40.57 (1.46)	
27.000	809.44	[CI] ($^3P_1$−$^3P_2$)	27.002	12.83 (1.43)	
27.208	815.68	HNC (9 − 8)	27.196	8.24 (5.70)	
27.693	830.22	$^{13}CH^+$ (1 − 0)	27.719	9.55 (2.35)	
27.857	835.13	CH^+ (1 − 0)	27.852	33.57 (1.46)	
27.963	838.31	N_2H^+ (9 − 8)	27.954	28.08 (1.54)	
28.168	844.46	H I (26 − 24)	28.180	21.11 (1.43)	
28.585	856.96	H I (30 − 27)	28.594	17.17 (1.42)	
28.789	863.07	$H^{13}CN$ (10 − 9)	28.786	9.32 (1.42)	
28.985	868.95	^{13}CN (8 − 7)	28.983	8.12 (1.62)	
29.038	870.54	$HN^{13}C$ (10 − 9)	29.059	8.07 (1.60)	
29.396	881.27	^{13}CO (8 − 7)	29.392	19.55 (1.42)	
29.553	885.98	HCN (10 − 9)	29.531	17.63 (1.43)	
29.622	888.05	H I (20 − 19)	29.635	104.90 (1.68)	
29.739	891.55	HCO^+ (10 − 9)	29.736	12.25 (1.44)	
30.094	902.20	NH_2 2(02)−1(11)	30.091	16.53 (4.33)	
30.244	906.69	CN (8 − 7)	30.250	41.00 (4.54)	bl. HNC (10 − 9)
30.269	907.44	NH_2 2(02)−1(11)			Weak
30.326	909.15	NH_2 2(02)−1(11)	30.330	15.85 (4.55)	
30.748	921.80	CO (8 − 7)	30.743	62.49 (4.31)	
31.068	931.40	N_2H^+ (10 − 9)	31.072	31.86 (4.31)	
31.410	941.65	NH_2 3(21)−3(12)			Weak
31.571	946.47	NH (1 − 0)	31.524	10.48 (2.69)	
31.613	947.73	NH_2 3(21)−3(31)	31.577	69.50 (2.52)	
31.665	949.29	$H^{13}CN$ (11 − 10)	31.664	12.98 (1.63)	
31.774	952.56	NH_2 1(11)−0(00)	31.778	38.58 (1.62)	
31.819	953.91	NH_2 3(21)−3(31)			Weak
31.846	954.72	H I (25 − 23)	31.858	30.19 (1.62)	bl. H I (29 − 26)
31.938	957.48	$HN^{13}C$ (11 − 10)			Weak
32.006	959.52	NH_2 1(11)−0(00)	31.999	36.87 (1.55)	
32.180	964.73	NH_2 3(12)−3(03)	32.158	7.34 (1.57)	
32.257	967.04	NH_2 3(12)−3(03)	32.257	17.85 (1.59)	
32.382	970.79	NH_2 3(12)−3(03)	32.356	21.87 (1.57)	
32.505	974.48	NH (1 − 0)	32.495	258.90 (2.30)	bl. HCN (11 − 10)
32.610	977.62	^{13}CN (9 − 8)	32.565	75.04 (2.00)	
32.711	980.65	HCO^+ (11 − 10)	32.678	12.05 (1.55)	
32.930	987.22	NH_2 2(20)−2(11)	32.937	16.28 (1.55)	
33.067	991.32	^{13}CO (9 − 8)	33.052	27.44 (1.63)	bl. H_2O 2(02)−1(11)

Table A1 – *continued*

Wavenumber (cm^{-1})	Frequency (GHz)	Identification (cm^{-1})	Measured ($10^{-17}Wm^{-2}$)	Line Flux	Comments
33.134	993.33	NH_2 2(20)−2(11)	33.135	20.51 (1.63)	
33.249	996.78	HNC (11 − 10)	33.261	21.67 (1.64)	
33.356	999.99	NH (1 − 0)	33.349	193.30 (1.93)	
33.456	1002.99	NH_2 2(20)−2(11)	33.431	42.86 (1.69)	
33.558	1006.04	NH_2 4(20)−4(13)			Weak
33.662	1009.16	NH_2 2(20)−2(11)			Weak
33.775	1012.55	NH^+ (3/2 − 1/2)	33.765	19.09 (1.06)	bl. NH_2 4(22)−4(13)
33.923	1016.99	NH_2 4(22)−4(13)	33.922	13.48 (1.07)	
34.021	1019.92	CN (9 − 8)	34.018	20.14 (1.07)	
34.172	1024.45	N_2H^+ (11 − 10)	34.168	24.33 (1.06)	bl. NH_2 4(22)−4(13)
34.588	1036.92	CO (9 − 8)	34.581	83.35 (1.09)	bl. $H^{13}CN$ (12 − 11)
34.695	1040.13	H I (19 − 18)	34.713	181.50 (1.22)	
34.838	1044.42	$HN^{13}C$ (12 − 11)			Weak
35.457	1062.97	HCN (12 − 11)	35.452	29.71 (1.08)	
35.589	1066.93	H I (28 − 25)	35.617	17.38 (1.55)	bl. HCO^+ (12 − 11)
36.194	1085.07	H I (24 − 22)	36.206	38.53 (1.27)	bl.^{13}CN (10 − 9)
36.268	1087.29	HNC (12 − 11)	36.280	15.16 (1.20)	
36.604	1097.36	H_2O 3(12)−3(03)	36.597	18.06 (1.14)	
36.737	1101.35	^{13}CO (10 − 9)	36.732	30.52 (1.06)	
37.137	1113.34	H_2O 1(11)−0(00)	37.162	13.80 (0.96)	
37.275	1117.48	N_2H^+ (12 − 11)	37.268	33.47 (0.83)	bl. NH_2 3(12)−2(21)
37.416	1121.70	$H^{13}CN$ (13 − 12)	37.413	19.84 (0.82)	
37.602	1127.28	NH_2 3(12)−2(21)	37.593	13.31 (0.81)	
37.737	1131.33	$HN^{13}C$ (13 − 12)	37.716	11.99 (0.90)	
37.796	1133.10	CN (10 − 9)	37.791	21.99 (0.91)	
38.426	1151.98	CO (10 − 9)	38.419	125.60 (0.97)	bl. HCN (13 − 12)
38.464	1153.12	H_2O 3(12)−2(21)			Weak
38.651	1158.73	HCO^+ (13 − 12)	38.673	10.50 (0.87)	
38.791	1162.93	H_2O 3(21)−3(12)	38.777	11.08 (1.19)	
38.975	1168.44	NH_3 (2 − 11)	38.973	19.54 (0.81)	
39.286	1177.76	HNC (13 − 12)	39.284	16.17 (0.82)	
39.840	1194.37	^{13}CN (11 − 10)			Weak
39.963	1198.06	H I (27 − 24)	39.969	25.14 (1.54)	
40.290	1207.86	$H^{13}CN$ (14 − 13)	40.283	23.48 (1.55)	
40.406	1211.34	^{13}CO (11 − 10)	40.391	66.85 (1.56)	bl. N_2H^+ (13 − 12)
40.523	1214.85	NH_3 (2 − 10)	40.524	42.22 (1.54)	
40.635	1218.21	$HN^{13}C$ (14 − 13)			Weak
40.996	1229.03	H I (18 − 17)	41.021	301.80 (1.85)	bl. H_2O 2(20)−2(11)
41.372	1240.30	H I (23 − 21)	41.374	65.27 (1.07)	bl. HCN (14 − 13)
41.570	1246.24	CN (11 − 10)	41.567	24.02 (1.05)	
41.620	1247.74	HCO+ (14 − 13)			Weak
41.682	1249.59	$H^{37}Cl$ (2 − 1)	41.669	20.16 (1.08)	
41.744	1251.45	HCl (2 − 1)	41.753	30.09 (1.09)	
42.263	1267.01	CO (11 − 10)	42.263	109.20 (1.12)	bl. HNC (14 − 13)
43.162	1293.96	$H^{13}CN$ (15 − 14)	43.159	19.95 (1.04)	
43.479	1303.47	N_2H^+ (14 − 13)	43.476	27.72 (1.06)	bl. ^{13}CN (12 − 11)
43.532	1305.06	$HN^{13}C$ (15 − 14)			Weak
44.073	1321.28	^{13}CO (12 − 11)	44.068	32.23 (1.05)	
44.308	1328.32	HCN (15 − 14)	44.304	26.08 (1.04)	
44.588	1336.71	HCO^+ (15 − 14)			Weak
45.085	1351.61	H I (26 − 23)	45.087	34.86 (1.05)	
45.342	1359.32	CN (12 − 11)	45.324	24.68 (1.05)	bl. HNC (15 − 14)
46.034	1380.06	$H^{13}CN$ (16 − 15)	46.012	27.18 (1.07)	
46.098	1381.98	CO (12 − 11)	46.099	125.70 (1.18)	bl. NH_2 2(21)−2(12)
46.428	1391.88	$HN^{13}C$ (16 − 15)			Weak
46.580	1396.43	N_2H^+ (15 − 14)	46.597	21.13 (7.46)	bl. NH_2 2(21)−2(12)
46.664	1398.95	NH_2 2(21)−2(12)			Weak
46.679	1399.40	NH_2 4(14)−4(04)			Weak
47.075	1411.27	^{13}CN (13 − 12)			Weak
47.256	1416.70	HCN (16 − 15)	47.254	39.88 (4.32)	
47.587	1426.62	H I (22 − 20)	47.602	66.23 (4.33)	bl. HCO^+ (16 − 15)
47.738	1431.15	^{13}CO (13 − 12)	47.750	53.88 (4.32)	bl. NH_2 4(13)−4(04)
47.892	1435.77	NH_2 4(13)−4(04)	47.899	28.10 (4.33)	

Table A1 *– continued*

Wavenumber (cm^{-1})	Frequency (GHz)	Identification (cm^{-1})	Measured ($10^{-17}Wm^{-2}$)	Line Flux	Comments
47.987	1438.61	NH_2 4(13)−4(04)			Weak
48.072	1441.16	NH_2 4(13)−4(04)			Weak
48.154	1443.62	NH_2 2(12)−1(01)	48.156	57.01 (4.36)	
48.268	1447.04	NH_2 2(12)−1(01)	48.289	57.03 (4.35)	
48.303	1448.09	NH_2 2(12)−1(01)			Weak
48.333	1448.99	HNC (16 − 15)			Weak
48.738	1461.13	[N II] ($^3P_0$−$^3P_1$)	48.726	543.40 (6.99)	
48.921	1466.61	H I (17 − 16)	48.953	479.40 (4.83)	bl. $H^{13}CN$ (17 − 16)
49.108	1472.22	CN (13 − 12)	49.081	24.10 (4.50)	
49.323	1478.67	$HN^{13}C$ (17 − 16)			Weak
49.679	1489.34	N_2H^+ (16 − 15)	49.682	16.50 (4.41)	
49.932	1496.92	CO (13 − 12)	49.929	134.00 (4.39)	
50.203	1505.05	HCN (17 − 16)	50.204	53.64 (4.33)	
50.521	1514.58	HCO^+ (17 − 16)			Weak
51.123	1532.63	H I (25 − 22)	51.143	54.57 (4.29)	
51.346	1539.31	HNC (17 − 16)			Weak
51.402	1540.99	^{13}CO (14 − 13)	51.409	52.96 (4.38)	

This paper has been typeset from a TEX/LATEX file prepared by the author.